Wave Boundary Layer Hydrodynamics and Sheet Flow Properties under Large-Scale Plunging-Type Breaking Waves

Guillaume Fromant, David Hurther, Joep van Der Zanden, Dominic A. van Der A, Ivan Caceres, Tom O'Donoghue, Jan S. Ribberink

Journal of Geophysical Research: Oceans

RESEARCH ARTICLE
10.1029/2018JC014406

Wave Boundary Layer Hydrodynamics and Sheet Flow Properties Under Large-Scale Plunging-Type Breaking Waves

G. Fromant[1], D. Hurther[1], J. van der Zanden[2], D. A. van der A[3], I. Cáceres[4], T. O'Donoghue[3], and J. S. Ribberink[2]

[1]Laboratory of Geophysical and Industrial Fluid Flows (LEGI),CNRS-Grenoble INP-UGA, Grenoble, France, [2]Department of Water Engineering and Management, University of Twente, Enschede, The Netherlands, [3]School of Engineering, University of Aberdeen, Aberdeen, UK, [4]Laboratori d'Enginyeria Maritima, Universitat Politècnica de Catalunya, Barcelona, Spain

Key Points:
- Wave velocity asymmetry transformation into near-bed wave velocity skewness occurs inside the WBL all across the studied wave-breaking region
- In the shoaling zone, the sheet flow sand transport rate exhibits a skewness driven contribution with negligible phase-lagging effects
- In the outer surf zone, a vertical three-layer structure of the (wave-, undertow-, and turbulent-driven) sheet flow sand fluxes is found

Correspondence to:
G. Fromant,
guillaume.fromant@univ-grenoble-alpes.fr

Citation:
Fromant, G., Hurther, D., van der Zanden, J., van der A, D. A., Cáceres, I., O'Donoghue, T., & Ribberink, J. S. (2019). Wave boundary layer hydrodynamics and sheet flow properties under large-scale plunging-type breaking waves. *Journal of Geophysical Research: Oceans*, *124*. https://doi.org/10.1029/2018JC014406

Received 26 JUL 2018
Accepted 8 DEC 2018
Accepted article online 11 DEC 2018

Abstract Wave boundary layer (WBL) dynamics are measured with an Acoustic Concentration and Velocity Profiler (ACVP) across the sheet flow-dominated wave-breaking region of regular large-scale waves breaking as a plunger over a developing breaker bar. Acoustic sheet flow measurements are first evaluated quantitatively in comparison to Conductivity Concentration Meter (CCM+) data used as a reference. The near-bed orbital velocity field exhibits expected behaviors in terms of wave shape, intrawave WBL thickness, and velocity phase leads. The observed fully turbulent flow regime all across the studied wave-breaking region supports the model-predicted transformation of free-stream velocity asymmetry into near-bed velocity skewness inside the WBL. Intrawave concentration dynamics reveal the existence of a lower pickup layer and an upper sheet flow layer similar to skewed oscillatory sheet flows, and with similar characteristics in terms of erosion depth and sheet flow layer thickness. Compared to the shoaling region, differences in terms of sheet flow and hydrodynamic properties of the flow are observed at the plunge point, attributed to the locally enhanced wave breaker turbulence. The ACVP-measured total sheet flow transport rate is decomposed into its current-, wave-, and turbulence-driven components. In the shoaling region, the sand transport is found to be fully dominated by the onshore skewed wave-driven component with negligible phase lag effects. In the outer surf zone, the total net flux exhibits a three-layer vertical structure typical of skewed oscillatory sheet flows. However, in the present experiments this structure originates from offshore-directed undertow-driven flux, rather than from phase lag effects.

Plain Language Summary We focus here on novel wave boundary layer hydrodynamics and sheet flow properties obtained with the Acoustic Concentration and Velocity Profiler measurement technology. It is the first time this advanced acoustic instrumentation is used for high-resolution measurements of wave-driven sheet flows under large-scale breaking waves. The wave boundary layer hydrodynamics and, in particular, the detailed properties of the sheet flow dynamics in terms of pickup layer, bedload, and suspended sand transport are investigated. Finally, sand fluxes (as transport rates) decomposed into the undertow-, the wave- and the turbulence-driven contributions allow a new insight into the underlying sand transport mechanisms in the scientifically challenging, coastal wave-breaking region. These results are compared to sheet flow properties obtained in (nonbreaking) oscillatory flows (from experiments in U-tube facilities) in order to show how the wave-breaking process impacts the internal and external sheet flow dynamics.

1. Introduction

Over the past decades, considerable research efforts have been concerned with understanding and modeling nearshore sand transport processes under energetic wave forcing conditions for which the sediment transport occurs as sheet flow. Previous studies on sheet flow processes were primarily conducted in flow tunnels (Dibajnia & Watanabe, 1998; Dick & Sleath, 1992; Hassan & Ribberink, 2005; Horikawa et al., 1982; McLean et al., 2001; O'Donoghue & Wright, 2004a, 2004b; Ribberink & Al-Salem, 1994; Ruessink et al., 2011; Sumer et al., 1996; van der A et al., 2010), in large wave flumes involving nonbreaking surface gravity waves over horizontally flat sand beds (Dohmen-Janssen & Hanes, 2002, 2005; Schretlen et al., 2009), or in the shoaling zone of a fixed bar composed of a mobile sand bed part as the test section (Anderson et al.,

2017; Mieras et al., 2017a). These experimental studies have revealed the complex structure of the internal sheet flow velocity, concentration, and sand flux (i.e., inside the bottom wave boundary layer, WBL) for a wide range of flow and sediment characteristics, while various process-based numerical models (Amoudry et al., 2008; Caliskan & Fuhrman, 2017; Cheng et al., 2017; Finn et al., 2016; Fuhrman et al., 2013; Hsu & Liu, 2004; Kranenburg et al., 2013, 2014) reproduce the dominant processes to a greater or lesser extent. These experimental and numerical studies have further led to the development of semiempirical, parameterized sand transport models for practical applications (e.g., Dibajnia & Watanabe, 1998; Drake & Calantoni, 2001; Fernández-Mora et al., 2015; Hoefel & Elgar, 2003; Nielsen, 2006; van der A et al., 2010, 2013; Watanabe & Sato, 2004) in which the key hydrodynamic WBL parameters are identified as the WBL thickness, the velocity phase lead, and the wave nonlinearities (velocity skewness and asymmetry), because they control the intrawave and net bed shear stress dynamics (Fuhrman et al., 2009; van der A et al., 2011) as the main driving force for bedload sand transport models.

The very limited number of internal sheet flow studies addressing both WBL hydrodynamics and sediment transport properties were primarily conducted in oscillatory flow tunnels (O'Donoghue & Wright, 2004a, 2004b) or under nonbreaking or shoaling waves (Anderson et al., 2017; Dohmen-Janssen & Hanes, 2002, 2005; Mieras et al., 2017a; Schretlen et al., 2009). The applicability of these results and proposed models to breaking wave conditions is still an open scientific question. In particular, the potential impact of the breaking-induced jet and bore turbulence on the key WBL hydrodynamic parameters and the internal sheet flow layer structure remains nonelucidated.

Only recently, van der Zanden, van der A., et al. (2017) estimated the cross-shore bedload transport over the entire wave-breaking region. That study quantified the contribution of bedload transport to the total transport in the cross-shore region extending from the wave shoaling zone to the inner surf zone. Bedload transport under sheet flow conditions was shown to dominate the total sand flux in the shoaling zone and in the outer surf zone, corresponding to the offshore face, crest, and upper onshore face of the breaker bar. In this region, sheet flow dominates the net onshore-directed sand transport, while undertow-driven, offshore-directed suspended transport dominates in the region shoreward of the bar slope. In van der Zanden, van der A., et al. (2017), depth-integrated bedload transport was estimated indirectly from the difference between total net transport rates (obtained from bed profile measurements) and measured net suspended transport rates. The internal structure of the sheet flow layer in terms of the key WBL hydrodynamic parameters (WBL thickness, velocity phase lead, and wave velocity nonlinearities), the sediment concentration, and sediment flux dynamics, at both intrawave and wave-averaged time scales, was not addressed in detail.

The present study focuses on WBL hydrodynamics and sheet flow transport processes using time-resolved, vertical profiling of colocated sand velocity, sand concentration, and bed level position, provided by the Acoustic Concentration and Velocity Profiler (ACVP) technology of Hurther et al. (2011). This high-resolution measurement technique has recently been applied to various process-oriented sediment transport studies (Cheng et al., 2017; Hurther & Thorne, 2011; Naqshband, Ribberink, Hurther, & Hulscher, 2014; Naqshband, Ribberink, Hurther, Barraud, et al., 2014; Revil-Baudard et al., 2015, 2016) directly providing sand flux profiles, which can be decomposed into turbulent, orbital wave and mean contributions for both bedload and suspended load. In the present study, the technology is applied for the first time to medium-sand sheet flow conditions, induced by large-scale breaking waves.

The experiments, data treatment, and validation of the measurements are described in section 2. Section 3 presents and discusses the WBL hydrodynamics in the wave-breaking region, with particular focus on (a) the free-stream wave characteristics, the intrawave orbital velocity field, (b) the intrawave WBL thickness, (c) the first harmonic and full harmonic velocity phase leads, and (d) the wave velocity nonlinearities (skewness and asymmetry) inside the WBL. The cross-shore variation in sheet flow properties are presented in section 4 with a focus on (a) intrawave concentrations, erosion depth, and sheet flow layer thickness and (b) the vertical structure of the sand flux.

2. Experimental Setup

2.1. Wave Conditions and Experimental Protocol

The experiments were carried out in the large-scale CIEM wave flume of the Universitat Politecnica de Catalunya in Barcelona (100-m long, 3-m wide, and 4.5-m deep), in which a breaker bar was generated by

monochromatic waves propagating over a beach comprising a well-sorted, medium sand (median diameter $d50$ = 0.249 mm, degree of uniformity σg = 1.36). The waves had period T = 4 s and wave height $H0$ = 0.85 m at the wave paddle, where the water depth was $h0$ = 2.55 m. Plunging breaking waves occurred at the breaker bar, consistent with the surf similarity parameter $\xi 0$ = 0.54 (Battjes, 1975).

The experimental facility and reference bed profile are presented in Figure 1. The break point and plunge point were located at x = 53 m and x = 55.5 m, respectively (van der Zanden et al., 2016; van der Zanden, Hurther, et al., 2017). In what follows, the x = 53 m location is used to define the separation of the shoaling and breaking zones. The present study concerns the sheet flow-dominated region on the bar extending from x = 51 m in the shoaling zone to the location of the plunge point at x = 55.5 m. The experimental protocol has been described in van der Zanden et al. (2016); therefore, only the main steps are summarized herein. The initial bed profile, that is, before waves, comprised a 1:10 offshore slope followed by an 18-m long horizontal test section where the water depth was 1.2 m. The reference barred profile shown in Figure 1a was produced by 105 min of waves propagating over the initial profile. The profile was drawn on both sidewalls of the flume in order to reshape the profile to this reference profile after each experiment. Each experiment lasted 90 min in total, comprising six 15-min runs, during which the breaker bar developed slowly. After every second run, that is, after 30 min, the bed profile was measured to track the morphological change and to estimate the total sand transport rate (from the morphological changes) across the entire wave-breaking region (van der Zanden, van der A, et al., 2017). After the last (sixth) run of each experiment, the flume was drained and the beach was reshaped back to the reference profile. This experimental protocol was repeated 12 times to enable measurements at 12 different cross-shore positions (shown in Figure 1b) along the same beach profile using the mobile measurement frame shown in Figure 1c.

2.2. Instrumentation

In the present paper we focus on the ACVP and the Conductivity Concentration Meter (CCM+) instruments. Two synchronized ACVPs were deployed, one was fixed at x = 54.5 m for comparison with CCM+ concentration measurements at the same position, and the other was deployed on the mobile frame to provide measurements at multiple locations along the barred profile. The ACVP instruments deliver quasi-instantaneous, simultaneous, and colocated 1-D vertical profiles of the two-component velocity field (streamwise and vertical velocity components u and w), together with the acoustic intensity profiles. The velocity components are extracted from the two quasi-instantaneous Doppler frequencies of the received acoustic pressure waves (Hurther et al., 2011). The acoustic intensity profiles are converted into mass concentration profiles using the incoherent acoustic inversion methods described in Hurther et al. (2011), Thorne et al. (2011), and Thorne and Hurther (2014). The present spatial and temporal resolutions are 1.5 mm and 1/70 s, respectively, over a maximum profiling range of 18 cm along the transmitter axis. The time-resolved near-bed sand flux profiles are calculated from the simultaneous colocated velocity and concentration profiles (Hurther & Thorne, 2011; Naqshband, Ribberink, Hurther, & Hulscher, 2014; Naqshband, Ribberink, Hurther, Barraud, et al., 2014; Revil-Baudard et al., 2015, 2016).

The CCM+ provides time-resolved sediment concentrations in the sheet flow layer from a point conductivity measurement (McLean et al., 2001; van der Zanden et al., 2015; van der Zanden, van der A., et al., 2017). The double probe technology of the CCM+ enables particle velocity estimation via signal cross-correlation techniques (McLean et al., 2001). The probe enters the sheet flow layer from a tank buried within the sand bed and samples the local conductivity at 1,000 Hz. Servomotors contained within the buried CCM tank can position the probe vertically with 100-μm accuracy. The system is equipped with a bed level tracking system that enables automatic repositioning of the probes at submillimeter accuracy to cover the entire sheet flow layer. Several hundred repeatable waves are required to profile the entire sheet flow layer and to give statistically converged concentrations and particle velocities. More details regarding the CCM+ and data processing can be found in van der Zanden et al. (2015), van der Zanden, van der A., et al. (2017).

2.3. Data Processing

Visual inspection of video records and analysis of water surface elevation measurements by van der Zanden et al. (2016) showed that the wave-breaking location varied over the first 5 min of each run. After this transient phase, the breaking location stabilized and a hydrodynamic equilibrium was established. Data

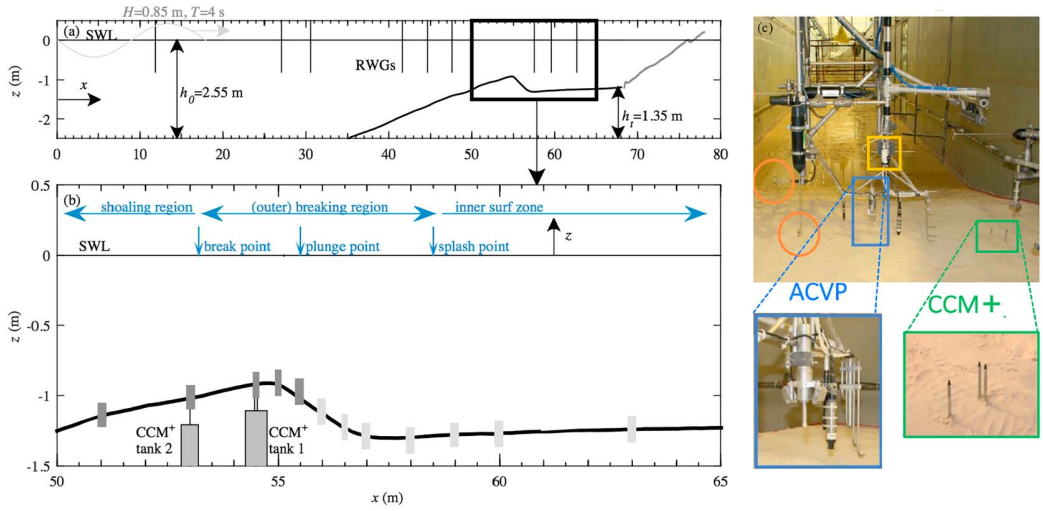

Figure 1. Experimental setup and measurement locations from van der Zanden et al. (2016). (a) Reference bed profile (black line) and fixed beach (gray line), locations of resistive wave gauges (vertical black lines); (b) positions of near-bed profiles measured with Acoustic Concentration and Velocity Profiler (ACVP, gray rectangles) and locations of the two CCM+ tanks. Dark gray profiles of ACVP show the investigated cross-shore positions herein; (c) mobile-frame photograph over the mobile bed showing the ACVP system and one of the two CCM+ systems. CCM+ = Conductivity Concentration Meter.

obtained during the first 5 min of each run were therefore discarded, leaving 10 min of data per run for processing and analysis, giving approximately 150 waves per run.

The inversion of the backscattered intensity recorded by the ACVP to give sediment concentrations followed the procedure described in Hurther et al. (2011) and the calibration method of Thorne and Hanes (2002) using the total suspended sediment (TSS) measured concentrations as reference data. For more details on the comparison between acoustically estimated and observed TSS, please refer to van der Zanden, van der A, et al. (2017).

Time-dependent ACVP measurements in the sheet flow layer are complicated by the fact that the no-flow bed level can gradually change during the measurement period due to large-scale bed level erosion or accretion. For example, at the start of an experiment prior to any wave action ($t < t_{start}$) the no-flow bed level might be detected at bin 60 in the ACVP profile (where bin 1 is closest to the emitter), while at the end of the run when the waves have stopped ($t > t_{stop}$) and the suspended sediment has settled, the bed could be detected at bin 64, meaning that there was an overall bed level erosion of four bin sizes, or 6 mm. In the analysis of their oscillatory flow tunnel measurements, O'Donoghue and Wright (2004a) assumed that throughout the experiment the no-flow bed level changed linearly in time, which allowed them to reference each bin at each time step to an instantaneous no-flow bed level, z(t) = 0. In this experiment the instantaneous undisturbed bed level ($z(t) = -\delta_e(t)$), was determined from the acoustic intensity profiles following the method of Hurther and Thorne (2011). By removing the intrawave variation from this instantaneous undisturbed bed level (by applying a low-pass filter with a cutoff frequency of $1/T = 1/4$ s = 0.25 Hz), the large-scale or gradual bed level change was obtained, which showed that the bed level did not always vary linearly in time. A somewhat different procedure compared to the linear interpolation by O'Donoghue and Wright (2004a) was therefore applied to determine instantaneous no-flow bed level. First, the distance, or "offset," between the no-flow bed level measured before the start of waves ($z(t < t_{start}) = 0$) and the filtered undisturbed bed level a few wave cycles after the wave paddle had started was determined. Second, the same offset between the filtered undisturbed bed level and the measured no-flow bed level after the wave paddle had stopped ($z(t > t_{stop}) = 0$) was determined. The offset was found to be the same at the start and end of every run and was approximately one bin size, or 1.5 mm, in length. Therefore, the no-flow bed level at every time step was established by assuming that the same constant offset applies throughout the run between the measured instantaneous large-scale undisturbed bed level and the instantaneous no-flow bed level. Following this procedure, every concentration and velocity measurement at every time step was associated with a particular elevation relative to the instantaneous no-flow bed level, which allowed subsequent phase averaging.

Table 1
Free-Stream Orbital Amplitude, Re and a/k_s for Each Cross-Shore Measurement Position Over the Complete Experiment (t = 0–90 min)

x (m)	51	53	54.5	55	55.5
a (m)	0.54	0.54	0.51	0.49	0.43
$Re/10^5$	6.2	6.0	5.6	5.0	3.8
$a/k_s/10^3$	1.8	1.8	1.7	1.6	1.4

To calculate the phase-averaged quantities, the wave-by-wave phase origin is taken as the zero up-crossing of the free-stream horizontal orbital velocity. The phase-averaged value of a variable ψ (which can be a function of z) is calculated over N repeated waves as $\psi(t/T) = \frac{1}{N}\Sigma_{n=1}^{N}\psi(t+(n-1)T)$. Decomposition into time-averaged ($\overline{\psi}$), orbital ($\widetilde{\psi} = \langle\psi\rangle - \overline{\psi}$) and turbulent contributions ($\psi' = \psi - \langle\psi\rangle$) is achieved following the method described in van der Zanden et al. (2016). Note that in the following, the terminology "intrawave" refers to variation of a phase-averaged quantity as a function of the relative phase t/T. For brevity, we omit the brackets $\langle\ldots\rangle$ to represent phase-averaged quantities in the remainder of this paper. Note that to facilitate comparisons of our phase-averaged results with previous sheet flow layer studies, a second vertical coordinate system, $z'(t)$, where $z'(t) = z(t) + \delta_e(t)$, is occasionally adopted in the remainder of this paper.

The intrawave top of the sheet flow layer (also called the suspension interface) was determined from the phase-averaged volumetric concentration using the criterion of 0.08 m^3/m^3 (Dohmen-Janssen et al., 2001) as the upper limit of the sheet flow layer. The CCM+ concentration measurements used to validate the acoustic measurements at 54.5 m (see next section) were averaged over at least 12 runs (of more than 100 waves per run), resulting in well-converged CCM+ phase-averaged concentrations, with negligible statistical bias error. The intrawave erosion depth and sheet flow layer thickness were obtained by applying the power law fitting method described in O'Donoghue and Wright (2004a) to the intrawave vertical profiles of concentration. The net sand transport rate (i.e., the time-averaged local flux vertically integrated over the sheet flow layer) is estimated from the particle velocity and concentration measurements, as detailed in van der Zanden, van der A., et al. (2017).

Velocity skewness and asymmetry are calculated as $Sk(u) = \overline{\widetilde{u}^3}/\widetilde{u}_{\mathrm{rms}}^3$ and $Asy(u) = -\overline{\mathscr{H}(\widetilde{u})^3}/\widetilde{u}_{\mathrm{rms}}^3$, where $\widetilde{u}$ is the (periodic) wave orbital velocity, $\widetilde{u}_{\mathrm{rms}}$ the root-mean-square periodic velocity, and $\mathscr{H}$ is the Hilbert transform (e.g., Elgar, 1987). Sk_∞ and Asy_∞ refer to velocity skewness and asymmetry values at the free-stream height (taken 0.1 m above the no-flow bed level as previously defined in van der Zanden et al., 2016).

Table 1 presents the orbital semiexcursion amplitude $a = \widetilde{u}_{\infty,\max}T/(2\pi)$ at the free-stream height normalized by the average bed roughness (k_s, using the formulation of van der A. et al., 2013), a/k_s, and the average Reynolds number $\mathrm{Re} = a\widetilde{u}_{\infty,\max}/\nu$, at each cross-shore position for the 27 successfully collected runs (3 runs out of 30 runs—6 runs times 5 cross-shore positions—failed due to acquisition problems) between x = 51 m and x = 55.5 m. Here ν is the kinematic viscosity of the fluid. Similar to van der Zanden et al. (2016), the free-stream height is taken at 0.1 m above the no-flow bed level, that is, well above the top of the bottom WBL (discussed in section 3.2). This height corresponds to a range of 5 to 10 times the local WBL thickness depending on the cross-shore position. Based on the Re and a/k_s values shown in Table 1, the flow regime is hydrodynamically fully turbulent and transitionally rough when compared to literature data in Jonsson (1980) and van der A et al. (2011; Figure 3).

2.4. Validation of ACVP Sheet Flow Measurements

In the present experiments, the ACVP technology was used for the first time under wave-driven sheet flow conditions with real sands. This experimental condition is different from previous studies in which the ACVP has been successfully used in gravity-current-driven sheet flows with light-weight particles (Fromant et al., 2018; Revil-Baudard et al., 2015, 2016). To assess the performance of the ACVP under these conditions, we compare ACVP-measured erosion depth, sheet flow layer thickness, and sand transport rate with the corresponding CCM+ measurements at x = 54.5 m.

Figure 2 presents the CCM+ and ACVP measurements for a representative run of the collected data set. Figures 2a and 2b show the ACVP-measured free-stream orbital velocity for reference. The shape of the free-stream velocity reveals strong positive velocity skewness and asymmetry typical of surf zone waves. Figures 2c and 2d show CCM+-measured (Figure 2c) and ACVP-measured (Figure 2d) $c(z,t/T)$, erosion depth $\delta_e(t/T)$, and suspension interface $\delta_u(t/T)$ (lower and upper white lines, respectively). Both instruments show similar intrawave dynamics: as seen from the CCM+ measurements, the bed is subject to deeper erosion under the wave crest than under the wave trough. The difference in erosion depth between the crest and trough is less than 1.5 mm and is therefore not resolved by the ACVP (which has a resolution of

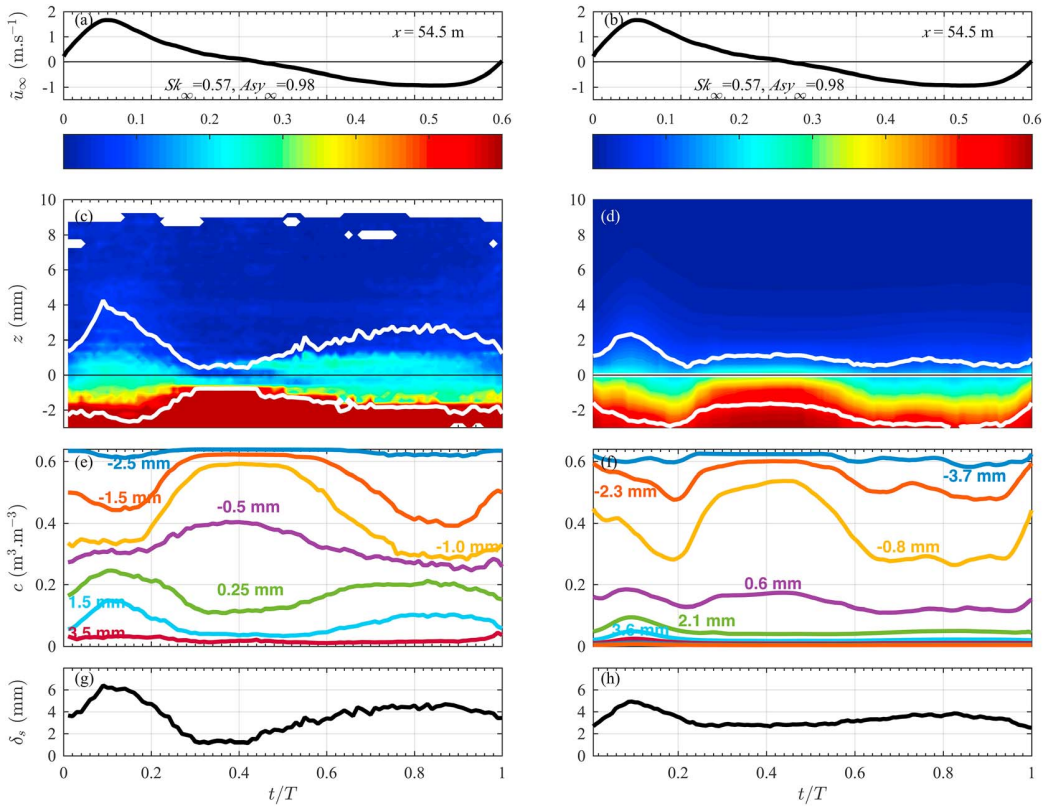

Figure 2. Intrawave Conductivity Concentration Meter (CCM+) and Acoustic Concentration and Velocity Profiler (ACVP) measurements at $x = 54.5$ m for final stage of bar development. (a, b) ACVP-measured orbital velocity at free-stream elevation, including velocity skewness (Sk_∞) and asymmetry (Asy_∞) values. (c) CCM+ and (d) ACVP concentration (in m^3/m^3) with white lines indicating the erosion depth and the top of the sheet flow layer; (e) CCM+ and (f) ACVP concentration at fixed elevations inside the sheet flow layer; (g) CCM+ and (h) ACVP intrawave sheet flow layer thickness.

1.5 mm). Both measurements show nonzero erosion depth at the two flow reversals, a consequence of nonsettled sediment load due to phase lag effects or non-locally controlled cross-shore sand advection processes. The suspension interface $\delta_u(t/T)$ reaches higher levels under the wave crest than under the wave trough, due to the stronger sand particle entrainment from the pickup layer. The existence of the pickup layer is seen from the $c(t/T)$ at selected elevations (Figures 2e and 2f): within the pickup layer, $c(t/T)$ is in antiphase with $\widetilde{u}_\infty(t/T)$ (Figures 2a and 2e), while in the upper sheet flow layer $c(t/T)$ and $\widetilde{u}_\infty(t/T)$ are in phase. Finally, the sheet flow layer thickness, $\delta_s(t/T)$, calculated as $\delta_u(t/T) - \delta_e(t/T)$, shows similar intrawave behavior between the two measurements (Figures 2g and 2h), with a thicker layer under the wave crest than under the wave trough, reflecting the differences in sand transport between crest and trough half cycles. In terms of quantitative comparison: CCM+ and ACVP maximum erosion depths are 2.7 mm and 2.9 mm, respectively, occurring at $t/T = 0.17$; maximum sheet flow layer thicknesses are 6 mm and 4.8 mm, respectively. Van der Zanden, van der A., et al. (2017) estimated a net bedload sand transport rate of 1.1×10^{-5} m^2/s based on the CCM+ measurements; the corresponding ACVP estimate (equations (5) and (7)) is $1.5\ (\pm 0.5) \times 10^{-5}$ m^2/s. Given the very different sampling and averaging techniques implemented by the two measurement systems, the relative difference of 25% between the CCM+ and ACVP net transport rates is considered as a satisfactory validation of the noninvasive acoustic sheet flow measurements used at all cross-shore positions in the following.

3. WBL Hydrodynamics

The present section focuses on the near-bed hydrodynamics across the sheet flow-dominated shoaling and breaking region (51 m $< x <$ 55.5 m) as determined from the ACVP measurements. The near-bed turbulence,

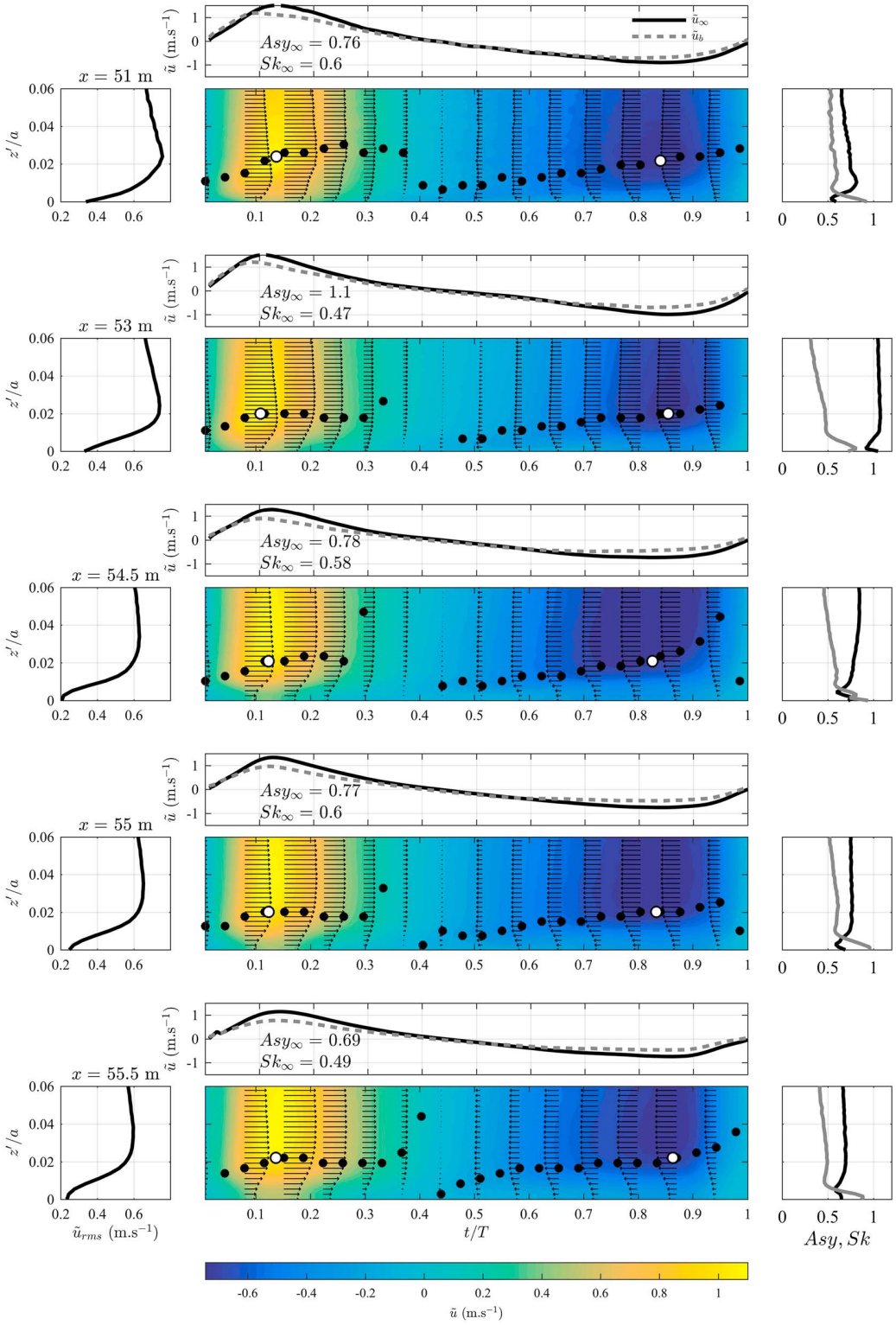

Figure 3. (left panels) Vertical profiles of $\widetilde{u}_{\text{rms}}$ velocity from $x = 51$ m (top) to $x = 55.5$ m (bottom); (right panels) profiles of asymmetry (black) and skewness (gray) from $x = 51$ m (top) to $x = 55.5$ m (bottom); (center panels) free-stream $\widetilde{u}_\infty(t/T)$ (black solid line) and near-bed $\widetilde{u}_b(t/T)$ intrawave velocities at $z' = 1.5$ mm (gray dashed line), and intrawave horizontal velocity field at each cross-shore position. Vertical profiles of wave velocity for 14 phases evenly separated over the wave period are shown (arrows), as well as the time-varying (black dots), crest and trough (white dots) wave boundary layer heights.

streaming, and undertow hydrodynamics were examined in van der Zanden et al. (2016) for the same experiment. The outer-flow hydrodynamics and turbulence were studied in van der A. et al. (2017) for identical wave conditions but over a fixed (immobile) breaker bar. Here we focus instead on the ACVP-measured wave-driven velocity field inside the bottom WBL. In particular, the cross-shore and intrawave variation in WBL thickness, velocity phase lead, and wave nonlinearities inside the WBL are analyzed and compared with previous results from oscillatory flow tunnel and nonbreaking wave experiments involving fixed and mobile beds. These hydrodynamic parameters all play a key role in the bed shear stress as the main driving forces in sheet flow sediment transport models (Drake & Calantoni, 2001; Hoefel & Elgar, 2003; Nielsen, 2006; Ribberink et al., 2008; van der A et al., 2010; Watanabe & Sato, 2004). The main objective of this section is to study how these hydrodynamic properties vary across the wave-breaking region.

3.1. Near-Bed Velocity Field

Figure 3 (left panels) presents the vertical profiles of $\widetilde{u}_{\mathrm{rms}}$ used for the detection of the bottom WBL. For comparison with O'Donoghue and Wright's (2004b) results for skewed oscillatory flows and van der A et al.'s (2011) results for asymmetric oscillatory flows, all vertical profiles in Figure 3 are bed referenced at intrawave scale before phase averaging, such that $z'/a = (z + \delta_e(t/T))/a$.

The left panels in Figure 3 show similar profile shapes of $\widetilde{u}_{\mathrm{rms}}$, including the presence of a typical near-bed velocity overshoot as a result of the bed friction-induced velocity-phase shifts inside the WBL (e.g., Nielsen, 1992). The top of the WBL, defined as the height of maximum overshoot in $\widetilde{u}_{\mathrm{rms}}$, is seen to increase with x over the range z'/a = [0.02–0.035]. The overshoot magnitude (x axis) in Figure 3 increases from x = 51 m to x = 53 m, decreases between x = 53 m and x = 54.5 m and varies slightly between x = 54 m and x = 55.5 m. This confirms that the investigated cross-shore domain includes the wave-breaking region associated with an abrupt reduction in wave energy.

The center panels of Figure 3 present $\widetilde{u}_{\infty}(t/T)$ and the near-bed velocity $\widetilde{u}_b(t/T)$ at z'_b = 1.5 mm ($z'/a \approx 0.003$), which corresponds to the first measurement point above the detected bed. For all cross-shore positions, the free-stream velocity is strongly positively skewed and asymmetric, with skewness and asymmetry values (noted in Figure 3, center panels) in the ranges Sk_{∞} = 0.47–0.6 and Asy_{∞} = 0.69–1.1, respectively. These values and their cross-shore variation are similar to values reported from previous wave flume experiments (Berni et al., 2013; Chassagneux & Hurther, 2014; Henriquez et al., 2014; Mieras et al., 2017a) and are slightly higher than values reported from field experiments (Doering & Bowen, 1995), the difference likely being due to the forced wave regularity and the flume-imposed shore-normal wave propagation direction.

The near-bed wave velocity fields represented by the color plots in the center panels of Figure 3 show an overall similar and typical near-bed intrawave behavior at all cross-shore positions with a region of overshoot in velocity amplitude above a region of velocity amplitude damping closer to the bed, as represented by the $\widetilde{u}_{\mathrm{rms}}$ profiles in the left panels of Figure 3. This characterizes the presence of a damped defect velocity oscillation propagating upward, typical of WBL hydrodynamics (Nielsen, 1992). The maximum wave velocity values are seen to increase between x = 51 m and x = 53 m and decrease toward the bar crest at x = 55 m as a consequence of the abrupt wave-breaking process initiated at x = 53 m.

3.2. Intrawave WBL Thickness

The intrawave boundary layer thickness δ_{WBL} is represented in Figure 3 by the black circle symbols in the velocity plots. It is calculated at each t/T as the distance between $z' = 0$ and the height where $\widetilde{u}\left(z'\right)$ is maximum and has the same sign as $\widetilde{u}(0)$ (Ruessink et al., 2011). For all cross-shore positions, the intrawave WBL thickness is seen to grow fairly linearly with time during the wave trough period associated with a favorable pressure gradient (for $0.4 < t/T < 0.83$, called the "wave back" by Henriquez et al., 2014). During the wave crest period with favorable pressure gradient (for $0 < t/T < 0.15$, the "wave front"), δ_{WBL} appears to grow linearly as well but at a faster rate. This higher WBL growth rate under the wave front relative to the wave back relates to acceleration skewness effects and was observed previously in asymmetric oscillatory flows (Ruessink et al., 2011; van der A et al., 2011) and in small-scale skewed asymmetric surface waves propagating over a fixed bar (Henriquez et al., 2014). Figure 3 further shows that slightly larger values of maximum intrawave WBL thickness are reached during the wave backs. This can also be observed from the difference in height between the two white dots in the color plots of Figure 3, corresponding to the associated crest

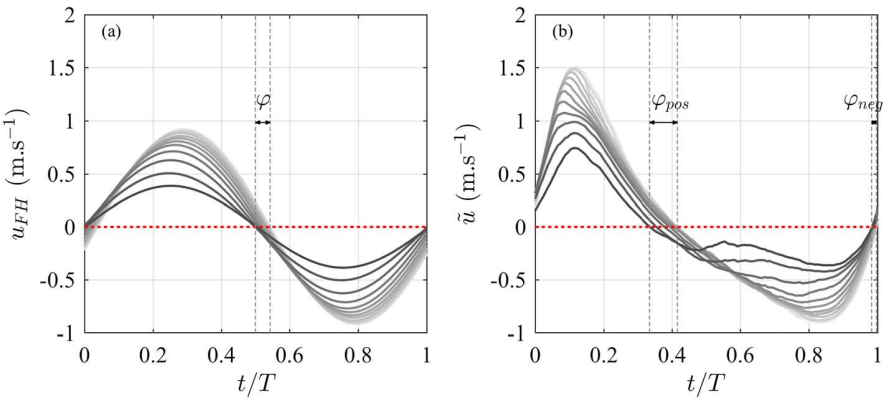

Figure 4. (a) First harmonic horizontal velocity u_{FH} from bed (dark gray) to free-stream elevations (light gray), indicating phase lead φ between free stream and near bed; (b) intrawave horizontal orbital velocity from bed (dark gray) to free-stream (light gray), indicating the positive-half cycle (φ_{pos}) and negative-half cycle (φ_{neg}) phase leads between free-stream and near-bed velocity x = 51 m.

and trough intrawave WBL thicknesses. This difference in maximum intrawave WBL thickness development during crest and trough was also observed by van der A et al. (2011) in fully turbulent asymmetric oscillatory flows and in Henriquez et al. (2014) for smooth-bed transitionally turbulent wave flume experiments.

3.3. WBL Phase Lead

The phase shift φ between the free-stream and near-bed wave velocities is another crucial WBL parameter controlling the phase at which the intrawave bed shear stress is maximum in the wave cycle. The near-bed velocity is known to lead the free-stream velocity with a value of $\varphi = 45^{\circ}$ in the case of laminar oscillatory flow and for very rough turbulent flows, such as oscillatory flows over vortex ripples (Nielsen, 2016). The phase lead reduces for increasing Reynolds number, due to the more effective turbulent momentum mixing (Nielsen, 1992). Accurate understanding and predictions of φ are important, because most quasi-steady bed-load sediment transport models use the intrawave bed shear stress, derived from the free-stream velocity, as the driving force for bedload sediment motion (Nielsen, 2006; Ribberink et al., 2008; van der A et al., 2013).

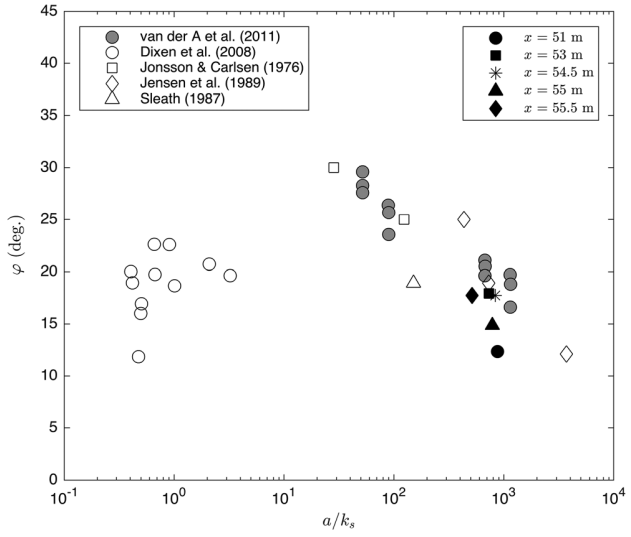

Figure 5. First harmonic phase leads observed at x = 51 m to x = 55.5 m as a function of a/k_s compared to existing studies (figure adapted from van der A et al., 2011).

Figure 4a shows an example of the increasing phase lead φ at x = 51 m between free-stream velocity and velocity at lower elevations, calculated from the first harmonic component of the wave velocity to enable rigorous comparison with previous oscillatory flow experiments.

Figure 5 shows φ at each cross-shore location (averaged over all runs at each location), in comparison with other WBL studies. When calculated for all 27 runs at all cross-shore positions as a function of the ratio a/k_s, the measured phase lead values (taken at 1.5 mm above the bed) vary between 8° and 20°, consistent with previous results for turbulent oscillatory flows. The new data provide additional supporting evidence that a logarithmic relation exists between φ and a/k_s for a/k_s larger than 10, as suggested by van der A et al. (2011). The small-scale wave flume data of Dixen et al. (2008) show that for very low a/ks values, which for their study were in the very rough turbulent regime, this logarithmic relationship does not apply.

Another interesting WBL aspect is the phase shift of the individual wave half cycles when all velocity harmonics are considered (see van der A et al., 2011). As shown in Figure 4b, for measurements at x = 51 m, the phase lead between the free-stream and near-bed velocities φ_{pos} at the crest-to-trough flow reversal is greater than the phase lead between the free-stream and near-bed velocities φ_{neg} at trough-to-crest flow reversal. The vertical profiles of phase lead are shown in Figure 6a for the cross-shore location with highest velocity asymmetry and lowest skewness

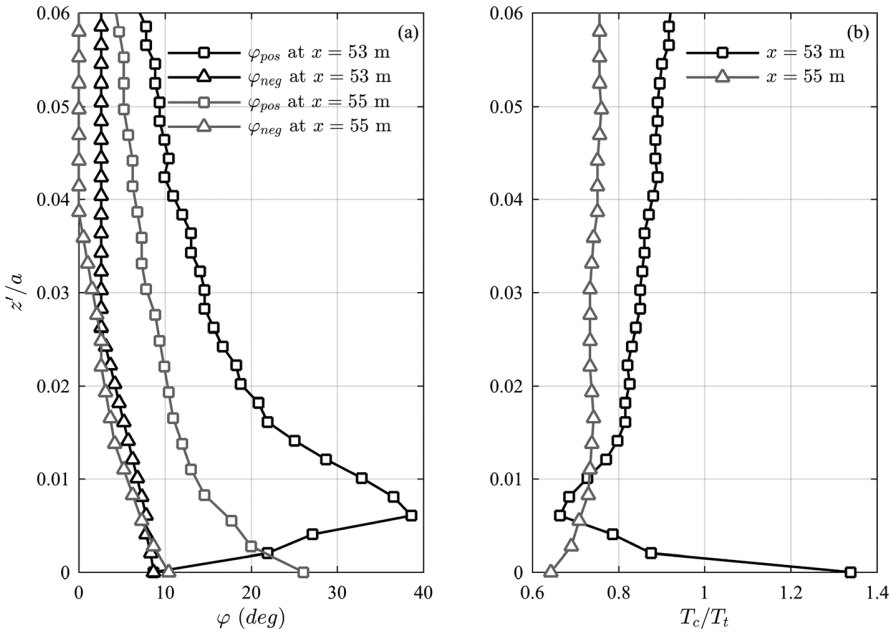

Figure 6. (a) Positive and negative half-cycle phase leads at $x = 53$ m and $x = 55$ m; (b) ratios of crest-to-trough durations T_c/T_t at $x = 53$ m and $x = 55$ m. Note that the free-stream elevation is at $z'/a \sim 0.2$.

($x = 53$ m at initiation of wave breaking) and the position with highest skewness and lowest asymmetry ($x = 55$ m, corresponding to the bar crest location). Figure 6b shows the corresponding profiles of orbital velocity crest-to-trough duration ratio T_c/T_t; this parameter is equal to one for nonskewed waves and decreases with increasing velocity skewness.

First, it can be seen that because of positively skewed free-stream velocities, $T_c/T_t<1$ for both $x = 53$ m and $x = 55$ m in Figure 6b, with a value closer to unity for $x = 53$ m compared to $x = 55$ m because of the lower free-stream velocity skewness at $x = 53$ m. Second, both profiles of φ_{neg} in Figure 6a are similar with weak vertical variation inside the WBL, whereas the profiles of φ_{pos} increase more strongly with proximity to the bed and reach maximum near-bed values of 38° and 25° at $x = 53$ m and $x = 55$ m, respectively. The difference between φ_{pos} and φ_{neg}, therefore, becomes stronger with proximity to the bed for $x = 53$ m. This is associated with a larger reduction in T_c/T_t as a consequence of the higher free-stream velocity asymmetry, hence a larger transformation of free-stream asymmetry into near-bed velocity skewness (addressed in detail in the following section). The correlation between the phase lead difference and the velocity skewness inside the WBL is in good agreement with the purely asymmetric conditions of van der A et al. (2011) with the difference that in the present study, the strong change in φ_{pos} is at the origin of the increasing phase shift difference, whereas in van der A et al. (2011) the difference was primarily due to a change in φ_{neg}. Another difference with van der A et al. (2011) is the nonmonotonic profile of φ_{pos} and T_c/T_t at $x = 53$ m reaching, respectively, a maximum and minimum value at $z'/a = 0.007$. This nonmonotonic trend in phase shift profile has also been observed by Ruessink et al. (2011) in oscillatory sheet flows. The trend results from the bed mobility, which causes the bed level to vary at the intrawave scale (discussed further in section 4). The nonmonotonic trend of T_c/T_t is a direct consequence of the trend observed on φ_{pos} profile.

Figure 7a presents the cross-shore evolution of maximum near-bed φ_{pos} and φ_{neg} values obtained from all experimental runs between $x = 51$ m and $x = 55.5$ m. The maximum values are used rather than the values at the same fixed near-bed position, because the elevations close to the undisturbed bed are affected by the bed mobility, as can be seen in Figure 6a for $x = 53$ m. These bed mobility-affected phase shift values are not representative of the WBL hydrodynamics and are therefore not used for comparison to the rigid-bed experiments. Figure 7b shows the corresponding free-stream velocity asymmetry, free-stream velocity skewness, and their ratio. It can be seen in Figure 7a that φ_{neg} has lower values (below 10°) and lower cross-shore variations than φ_{pos} across the shoaling and outer surf zone, with a gently monotonically

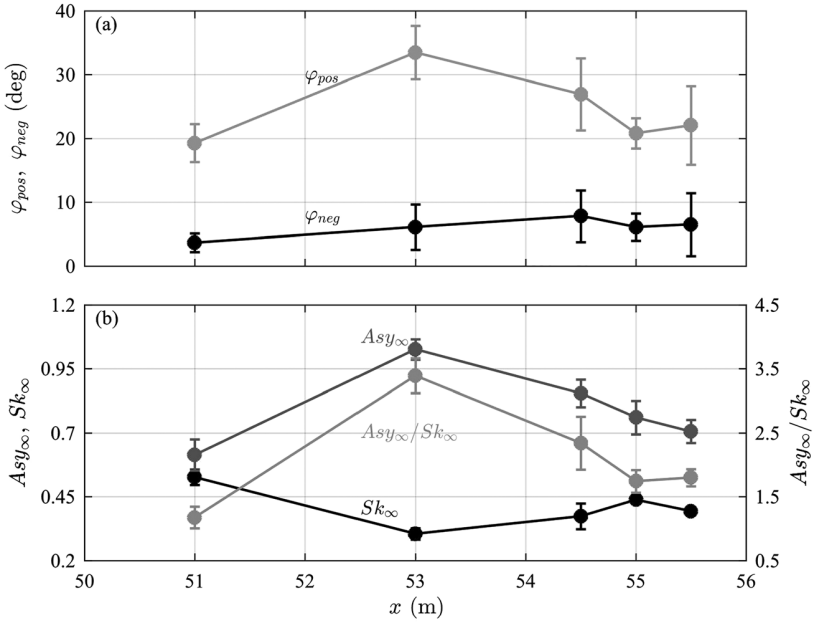

Figure 7. (a) Cross-shore variation of phase shifts φ_{pos} and φ_{neg} (maximum values in their near-bed profiles, as shown in Figure 6 for x = 53 m and x = 55 m) between x = 51 m and x = 55.5 m; (b) cross-shore evolution of Asy_∞, Sk_∞, and Asy_∞/Sk_∞ between x = 51 m and x = 55.5 m. Values are averaged over all runs per location with associated error bars marking ±1 standard deviation.

increasing trend with x. In contrast, φ_{pos} values are 2 to 3 times larger, with stronger nonmonotonic cross-shore variations compared to φ_{neg}. When compared to the cross-shore evolution of the free-stream parameters (Figure 7b), it can clearly be seen that the variation of the difference in φ_{pos} and φ_{neg} (as an indicator of near-bed velocity skewness) closely follows the cross-shore evolution of the ratio between free-stream velocity asymmetry and free-stream skewness rather than the individual parameters. This supports the existence of a relation between free-stream asymmetry and near-bed velocity skewness, and its potential prediction ability using nonlinear free-stream wave characteristics. This WBL mechanism is addressed in more details in the next section.

3.4. Wave Nonlinearities Inside the WBL

The onshore skewness of the horizontal free-stream wave velocity component is known to be the main contributor to the onshore skewness of the bed shear stress and hence driver for net onshore bedload transport (Bailard, 1981; King, 1991; Nielsen, 2006; Nielsen & Callaghan, 2003). On the other hand, as shown numerically by Fuhrman et al. (2009), the wave asymmetry effect (induced by the sawtooth wave shape) on the net onshore bedload transport has much less impact (even less than the bed slope effect due to the typical convergent shoaling bathymetry). For skewed asymmetric waves propagating across the shoaling and surf zones, the contribution to the net and skewness of the bed shear stress lies in-between the contribution of a purely skewed and a purely asymmetric wave field as demonstrated quantitatively in Fuhrman et al. (2009). However, the internal WBL mechanism leading to the (velocity asymmetry driven) onshore bedload sand transport has not been addressed. The WBL transformation of velocity asymmetry into bed velocity skewness proposed by Henderson et al. (2004) offers an interesting explanation of velocity asymmetry driven bed shear stress. Berni et al. (2013) simplified the model relating the ratio of near-bed to free-stream velocity skewness to the ratio of free-stream asymmetry to skewness:

$$\frac{Sk_b}{Sk_\infty} = \cos(\varphi) + \sin(\varphi)\frac{Asy_\infty}{Sk_\infty} \tag{1}$$

where φ corresponds to the first harmonic phase lead as defined in section 3.3. From a practical point of view, if valid, such a model offers the possibility to predict more accurately the intrawave orbital velocity at the bed. This could allow the use of a simple bedload transport model (without any parameterized WBL effects) as

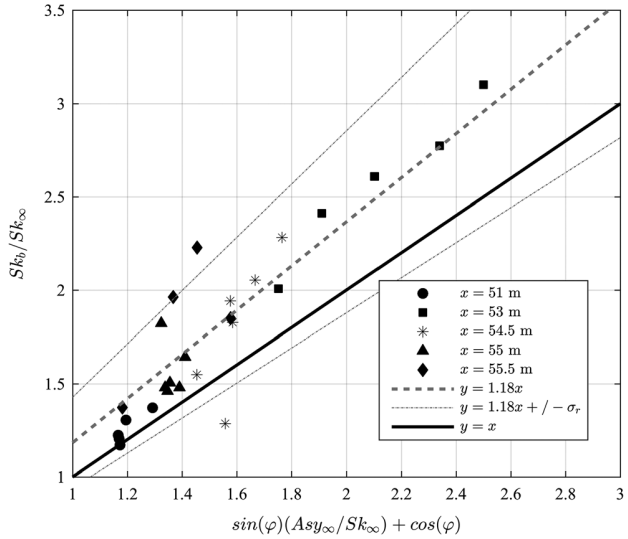

Figure 8. Sk_b/Sk_∞ against $\cos(\varphi) + \sin(\varphi)\frac{Asy_\infty}{Sk_\infty}$. The solid black line shows $Sk_b/Sk_\infty = \cos(\varphi) + \sin(\varphi)\frac{Asy_\infty}{Sk_\infty}$. The best least squares linear fit $Sk_b/Sk_\infty = 1.18\left[\cos(\varphi) + \sin(\varphi)\frac{Asy_\infty}{Sk_\infty}\right]$ is shown by the gray dashed line; gray dotted lines correspond to ±1 standard deviation off the best fit.

long as the velocity skewness at the bed is properly predicted by equation (1). The validity of equation (1) relies on the assumption of frequency independence of the phase lead and attenuation factor inside the WBL over the first three harmonics of the velocity. This model has been tested successfully for nonbreaking skewed asymmetric waves in low Reynolds number conditions (Henriquez et al., 2014) and for bichromatic waves at a single cross-shore position in the inner surf zone (Berni et al., 2013). While these previous experiments were conducted in small-scale wave flumes under lower Reynolds number conditions, the model is tested here for large-scale shoaling and breaking waves driving sheet flow transport.

Figure 3 (right panels) shows the vertical profiles of velocity skewness and asymmetry at all cross-shore positions. It can be seen that for all locations velocity skewness increases with proximity to the bed inside the WBL, while velocity asymmetry decreases with proximity to the bed. The largest near-bed to free-stream velocity skewness ratio ($Sk_b/Sk_\infty \simeq 2$) is found at x = 53 m, which corresponds to the position of the largest free-stream asymmetry to free-stream skewness ratio (shown in Figure 8b). This qualitatively suggests that the transformation of the wave nonlinearity inside the WBL follows the tendency given by equation (1). Furthermore, the skewness and asymmetry profiles measured in the present experiments are in close agreement with those obtained from previous small-scale wave flume measurements (Berni et al., 2013; Henriquez et al., 2014).

In order to test quantitatively equation (1) for the near-bed skewness prediction, Figure 8 shows the ratio of near-bed to free-stream velocity skewness, Sk_b/Sk_∞, against $\cos(\varphi) + \sin(\varphi)\frac{Asy_\infty}{Sk_\infty}$ for all runs across the studied wave-breaking region. The best least squares linear fit is $Sk_b/Sk_\infty = 1.18\left[\cos(\varphi) + \sin(\varphi)\frac{Asy_\infty}{Sk_\infty}\right]$, with a squared correlation coefficient R^2 = 0.84; it is represented as a dashed gray line in Figure 8. This corresponds to an 18% overestimation of the model-predicted values of near-bed velocity skewness. The line corresponding to equation (1) (solid black line) lies within the ±1 standard deviation (σ_r, represented as the two gray dotted lines) range around the best least squares linear fit. The lowest values of free-stream velocity asymmetry to skewness ratio are seen at x = 55 m (black triangles), which agrees with the position of lowest difference in phase leads φ_{pos} and φ_{neg} in Figure 7a. The largest ratio values in Figure 8 correspond to the runs at 53 m where the largest phase lead asymmetry is indeed observed in Figure 7a. The runs outside or closest to the 1 standard deviation limits (as the gray dashed dotted lines in Figure 8) are mainly at x = 55.5 m (black diamonds), suggesting that equation (1) is less robust in the vicinity of the plunge point within the outer surf zone. At this position, wave-breaking turbulence invades the WBL, as shown in van der Zanden, Hurther, et al., 2017; Figure 3c), affecting directly the orbital wave velocity field. When these outliers are excluded from the best fit, the linear regression has a squared correlation coefficient R^2 = 0.93. The observed 18% overestimation can also be attributed to the difficulty to accurately measure velocity skewness with an ACVP resolution of 1.5 mm in the near-bed region of strong vertical velocity gradient.

It can be concluded that the model of Henderson et al. (2004) gives a reasonable prediction of the near-bed velocity skewness across the sheet flow-dominated wave-breaking region.

4. Sheet Flow Sediment Dynamics

This section focuses on the detailed sheet flow sediment dynamics across the wave-breaking region and compares results against those obtained in previous large-scale oscillatory flow tunnel experiments (Dohmen-Janssen et al., 2001; Dohmen-Janssen & Hanes, 2002; Hassan & Ribberink, 2005; O'Donoghue & Wright, 2004a, 2004b; Ribberink & Al-Salem, 1994; van der A et al., 2010) and from large-scale nonbreaking surface wave experiments over horizontal sand beds (Dohmen-Janssen & Hanes, 2002; Ribberink et al., 2001; Schretlen, 2012; Schretlen et al., 2009). First, the intrawave and maximum erosion depth and sheet flow layer thickness are investigated and compared to predictions from existing empirical equations. Second, the

intrawave sediment concentration dynamics inside the sheet flow layer are explored, with particular focus on concentrations within the pickup layer and estimates of reference height and reference concentration. Whether wave breaking affects these internal sheet flow properties in comparison to oscillatory sheet flows is of specific interest here. Third, the intrawave and net sand flux and its decomposition into current, waveand turbulent contributions are examined. Finally, the ACVP-measured sheet flow transport rates across the wave-breaking region are compared to estimates of model-predicted net transport rates using a simple Meyer-Peter and Müller (1948)-type formulation.

4.1. Erosion Depth δ_e and Sheet Flow Layer Thickness δ_s

The erosion depth is measured directly from the undisturbed bed level detection performed with the ACVP (see section 2). This direct method differs from the one using concentration measurements obtained with conductivity-based technology, which relies on the fitting of a prescribed power law profile to the measured concentration profile (Lanckriet et al., 2014; Mieras et al., 2017a; O'Donoghue & Wright, 2004a; van der Zanden et al., 2015).

Figures 9a–9e present the intrawave erosion depth $-\delta_e(t/T)$ and the suspension layer interface $\delta_u(t/T)$ for the five locations of interest. For all locations, it can first be noticed that the erosion depth $-\delta_e(t/T)$ increases at the beginning of each flow half cycle as sediment is mobilized and reduces after maximum velocities have been reached and sediment is deposited. This general behavior of $-\delta_e(t/T)$ is qualitatively similar to measurements from the sheet flow experiments of O'Donoghue and Wright (2004a).

For velocity-skewed oscillatory flows, O'Donoghue and Wright (2004a) found shorter and slightly larger erosion to occur during the wave crest compared to longer and slightly smaller erosion during the wave trough. Figures 9 and 10 confirm this behavior for the present experiments at most locations (except at x = 54.5 m where erosion during crest and trough are of similar magnitude). However, it should be noted that the differences in erosion depths between crest and trough are small and within the margin of error (Figure 10).

The maximum intrawave erosion depth systematically lags the free-stream maximum velocity by about 20° (with a lag $\Delta t/T \approx 0.06$). This is reasonably close to the erosion depth phase lag obtained with the relation $\Phi_{\delta e} = 0.1\theta_{\max}$ of O'Donoghue and Wright (2004a), which gives here a maximum value of 15° for $\theta_{\max}$ = 2.5. The minimum values of intrawave erosion depth are about −1.5 mm and occur at crest-to-trough flow reversals for all positions.

The height of the suspension interface $\delta_u(t/T)$ is maximum at the phase of maximum velocity but is not zero at flow reversal, which might be due to (a) phase lag effects related to the settling suspended load or (b) nonlocal suspended sediment advection processes, as indicated in van der Zanden, Hurther, et al. (2017). The latter process is especially important at x = 55.5 m, where the local undisturbed bed level increases steadily between t/T = 0.2 and 0.4, that is, between the passage of the wave crest and flow reversal (Figure 9e). During this stage, horizontal sand influxes from adjacent onshore and offshore locations to x = 55.5 m lead to a local "compression" of suspended sand and to a net deposition (see van der Zanden, Hurther, et al., 2017; Figure 15). This only occurs at x = 55.5 m and not at the other locations, as seen in Figure 9, because this location is on the shoreward face of the breaker bar, where a strong undertow produces a large and steady offshore-directed suspended sand flux (van der Zanden, van der A, et al., 2017). Also note that despite phase leads of velocity near the bed, and the associated expected phase lead of the bed shear stress and pickup, the sheet flow layer thickness does not lead the free-stream velocity. This is physically explained because the total vertical flux resulting from pickup and sand settling fluxes becomes negative only after a certain time lag with respect to the instant of maximum pickup (Nielsen et al., 2002).

Figures 9f–9j show the intrawave sheet flow layer thickness (corresponding to the gray zone in Figures 9a–9e), estimated as $\delta_s(t/T) = \delta_e(t/T) + \delta_u(t/T)$. For all cross-shore positions, $\delta_s(t/T)$ is larger at wave crest than at wave trough. Similar to previous wave flume observations involving medium sand (Dohmen-Janssen & Hanes, 2002; Mieras et al., 2017a; Schretlen et al., 2009), the phase lag of $\delta_s(t/T)$ relative to free-stream velocity becomes negligible despite the weak phase lag seen in $\delta_e(t/T)$. The nonzero $\delta_s(t/T)$ at the flow reversals can be explained by the ongoing settling of the suspended sand at the flow reversals or by the steady sand advection induced by the undertow current as discussed above.

Based on oscillatory sheet flow measurements, empirical models have been proposed for maximum half-cycle erosion depth as a function of maximum half-cycle Shields number $\theta_{\max}$. As in van der Zanden et al.

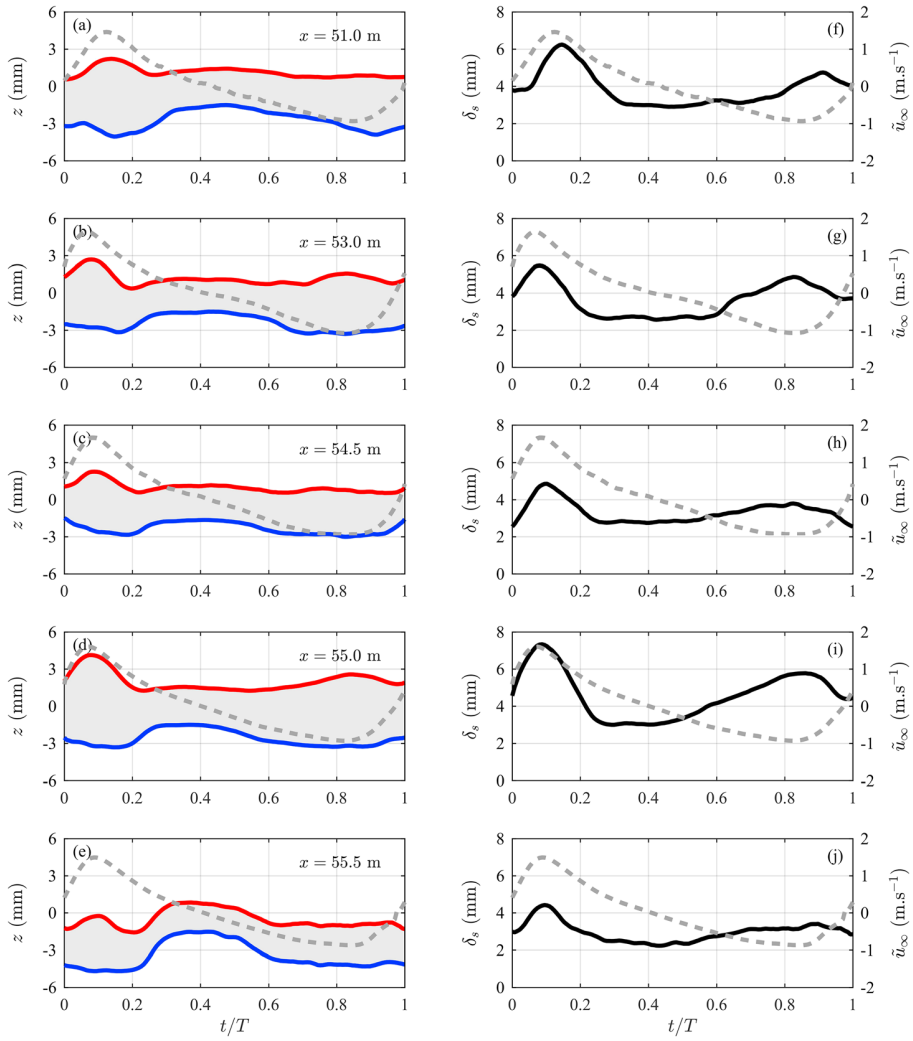

Figure 9. (left) Intrawave erosion depth $-\delta_e(t/T)$ (blue solid line), suspension layer (i.e., top of sheet flow layer, red solid line), and free-stream orbital velocity (gray dashed line) for x = 51 m (a) to x = 55.5 m (i). the gray-shaded parts of the figure represent the sheet flow layer; (right) corresponding time-varying sheet flow layer thickness $\delta_s(t/T)$ (black solid line) and free-stream orbital velocity (gray dashed line).

(2016), distinction is made between crest and trough erosion, $\delta_{e,\ \max}$ (crest) and $\delta_{e,\ \max}$(trough). The corresponding Shields number $\theta_{\max}$ at wave crest and trough are calculated using the methodology described in Ribberink (1998), which accounts for wave-plus-current contributions. The formulation proposed by Ribberink et al. (2008) is considered here:

$$\frac{\delta_{e,\max}}{d_{50}} = 3.7\ \theta_{\max} \tag{2}$$

Figure 10 compares measured $\delta_{e,\ \max}/d50$ values with those obtained using equation (2). Note that in this figure and similar ones presented later, we used a constant d_{50} = 0.249 mm for normalization at all cross-shore locations. Predictions obtained with equation (2) return an overall rather poor agreement with measured maximum erosion depth values, except for the crest erosion depths where the measurements broadly follow the prediction trend. The discrepancies between model estimates and measured values are largest for wave trough erosion depths, with smaller model predictions values. For most of these events, $\theta_{\max}$ is generally less than one, which corresponds to a transition regime between bedform and sheet flow transport. This interval lies outside the range of applicability of equation (2).

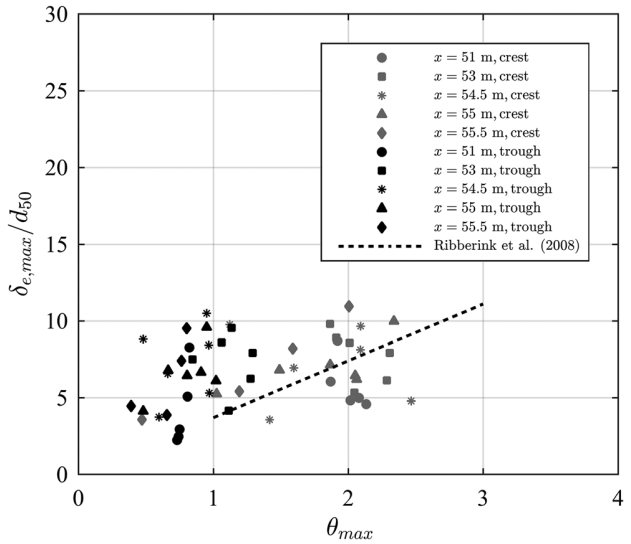

Figure 10. Maximum erosion depth versus maximum shields number per wave half cycle. Empirical relation proposed by Ribberink et al. (2008; equation (2), black dashed line) is included.

Similarly, sheet flow layer thickness $\delta_{s,\,\max}$ at wave troughs and crests are compared with values calculated using the empirical equation of Ribberink et al. (2008),

$$\frac{\delta_{s,\,\max}}{d_{50}} = 10.6\theta_{\max} \tag{3}$$

and Schretlen (2012),

$$\frac{\delta_{s,\,\max}}{d_{50}} = 13.1(\theta_{\max})^{0.7} \tag{4}$$

based on large-scale oscillatory flow tunnel and nonbreaking wave experiments, respectively.

Measured and predicted $\delta_{s,\,\max}$(crest) and $\delta_{s,\,\max}$(trough) are presented in Figure 11. As expected, measured and predicted values are in closest agreement at x = 51 m. At this location sand transport is controlled by local bed friction processes, with negligible impact from wave-breaking turbulence, as shown in van der Zanden et al. (2016). The largest scatter relative to the empirical formulae occurs for $\delta_{s,\,\max}$(crest) at x = 55 m and x = 55.5 m. This suggests a local impact of wave-breaking-induced turbulence, which was shown to be maximum at x = 56 m in van der Zanden et al. (2016).

4.2. Internal Sheet Flow Structure

The internal structure of the sheet flow layer and its cross-shore variation in the wave-breaking region are investigated on the basis of the intrawave and time-averaged concentration measurements and comparisons with corresponding observations from large-scale oscillatory flow tunnel experiments.

4.2.1. Pickup Layer

Figures 12a and 12b show an example of intrawave erosion depth with the corresponding intrawave concentrations at different elevations, respectively. As reviewed in Ribberink et al. (2008), oscillatory sheet flows exhibit a vertical two-layer structure, comprising a lower pickup layer and an upper sheet flow layer. In the pickup layer, sand grains constituting the moveable bed at rest are entrained as a consequence of bed erosion. As a result, with increasing flow velocity the local concentration decreases from the maximum value corresponding to the undisturbed bed concentration (close to 55% in volumetric concentration). This leads to an antiphase behavior between intrawave concentration and free-stream velocity (Ribberink et al., 2008). The upper sheet flow layer is defined as the flow region in which the intrawave sand concentration is in phase with the free-stream wave velocity, as a result of increasing sand entrainment into a region of negligible concentration when no flow is applied. As shown in O'Donoghue and Wright (2004a), the top of the pickup layer in oscillatory sheet flow is found to correspond to the elevation of minimum variation in intrawave concentration, separating the lower antiphase from the upper in-phase concentration layers.

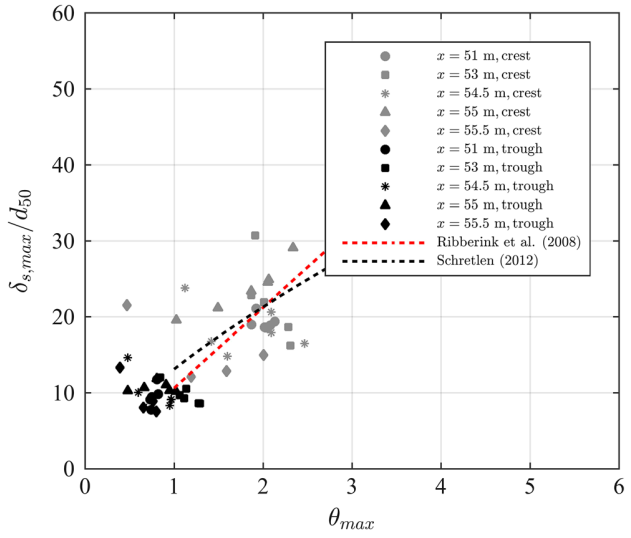

Figure 11. Maximum sheet flow layer thickness versus maximum shields number per wave half cycle. Empirical relations proposed by Ribberink et al. (2008; equation (3), red dashed line) and Schretlen (2012; equation (4), black dashed line) are included.

Figure 12c presents the vertical profile of the standard deviation of intrawave concentration normalized by the local mean concentration, $c_{\text{std}} = \text{std}(c)/\overline{c}$, at x = 54.5 m. It can be seen that at the maximum erosion depth of $z = -7$ mm, the intrawave concentration variation vanishes to zero. Above this position, a local minimum is found at $z = z_p \approx 0.6$ mm. This height corresponds to the top of the pickup layer, as verified in Figure 12d, which shows that this elevation corresponds to the pivot point of the concentration profile (normalized by the undisturbed bed concentration value $c_0 \approx 0.6$ m^3/m^3) separating the upper, in-phase layer and

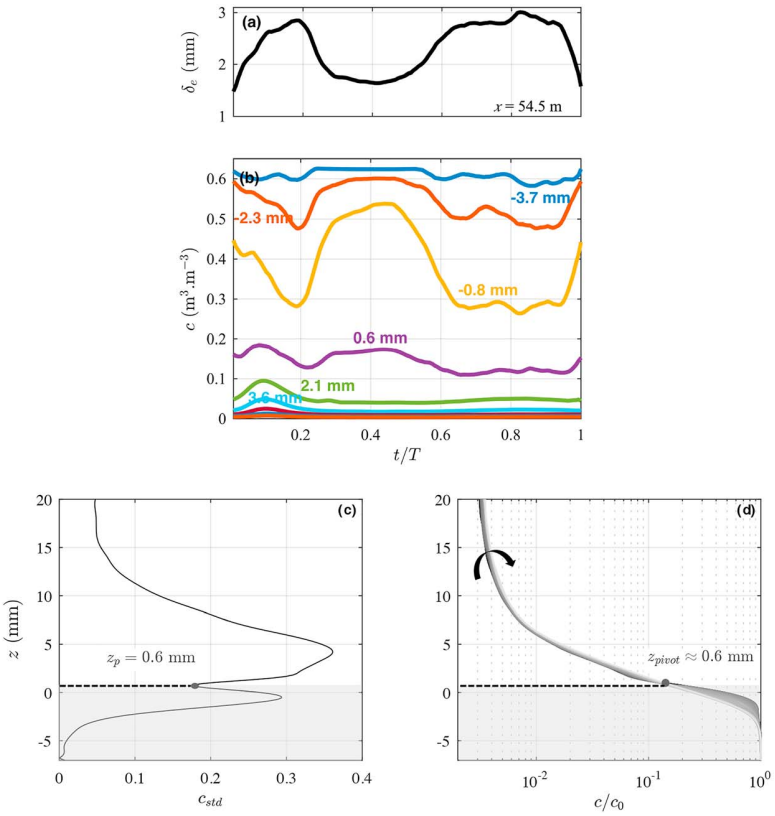

Figure 12. (a) Intrawave erosion depth δ_e at x = 54.5 m; (b) intrawave concentration at fixed elevations from the bed to the free-stream elevation at x = 54.5 m; (c) vertical profile of the (local mean concentration normalized) standard deviation of the concentration c_{std} at x = 54.5 m. The elevation of the local minimum (z_p) is indicated by the horizontal dashed line; (d) concentration profile clockwise pivoting as u and δ_e increase at x = 54.5 m. Pivot here is marked by a gray dot.

the lower, antiphase layer (O'Donoghue & Wright, 2004a). The vertical two-layer structure comprising lower pickup layer below the pivot level and upper sheet flow layer above the pivot level, found at x = 54.5 m, was observed for all other cross-shore positions. It appears that the sheet flow structure generated under shoaling and breaking waves is similar to that seen previously in oscillatory flow tunnel experiments (O'Donoghue & Wright, 2004a, 2004b).

4.2.2. Reference Height and Concentration

As proposed in O'Donoghue and Wright (2004a), the local minimum in c_{std} at the top of the pickup layer makes this height ideal for the reference height (z_p) and reference concentration (c_p) in concentration profile models. Moreover, the relative independency of the normalized pickup concentration $c_p \approx 0.44$ and height z_p with varying flow forcing and sediment properties reduces the number of model parameters to two (instead of three) as the erosion depth and the reference concentration values as shown in O'Donoghue and Wright (2004a).

To see if this model simplification also applies to our wave flume measurements, we investigate whether the pickup height z_p and normalized pickup concentration c_p have similar properties as in oscillatory flow tunnel sheet flows. Figure 13 presents the cross-shore variation of z_p and c_p. Mean z_p (Figure 13a) values, equal to the average value over all runs at each cross-shore position, vary between −0.5 mm and 1.5 mm. The z_p decreases between x = 51 m and x = 54.5 m and increases until the plunge point at x = 55.5 m. The corresponding cross-shore variation of c_p (Figure 13b) exhibits an opposite behavior: c_p increases from ≈0.5 to ≈0.6 between x = 51 m and x = 54.5 m and decreases abruptly at the plunge point. High spreading of both parameters is observed at x = 55 m, corresponding to the cross-shore position of highest horizontal gradients in near-bed velocity, as shown in van der Zanden et al. (2016). The strong cross-shore variability in reference height z_p and concentration c_p suggests that breaking-generated turbulence in the outer surf zone tends to

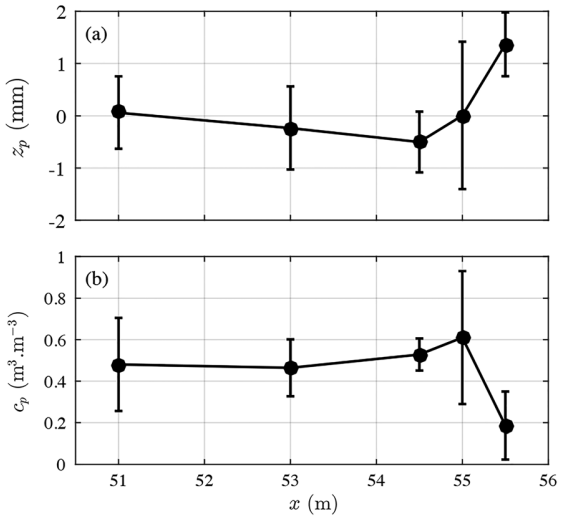

Figure 13. (a) Cross-shore variation of pickup height z_p; (b) cross-shore evolution of the reference concentration c_p values (a, b) are averaged over all runs with associated error bars marking ±1 standard deviation.

increase pickup heights with correspondingly lower reference concentration values, as a consequence of more effective (and temporally homogeneous) vertical turbulent sediment mixing. Compared to the fairly constant value of 0.44 found in oscillatory flow tunnel sheet flows by O'Donoghue and Wright (2004a), the observed c_p values of around 0.5 agree reasonably well for the cross-shore positions (x = 51 m to 55 m).

4.3. Sand Flux Dynamics

Figure 14 shows an example of the intrawave and time-averaged profiles of (wave plus current) horizontal velocity, concentration, and sand flux at x = 54.5 m. Here profiles are represented as a function of z, instead of z', in order to appreciate the intrawave bed erosion dynamics. The intrawave undisturbed bed level and the level of the suspension interface are also shown. The time-averaged velocity profile in Figure 14b shows the offshore-directed undertow profile above the WBL of about −0.3 m/s. Inside the sheet flow layer ($z<$ 5 mm), a weak WBL streaming can be seen, inducing a thin layer of onshore- and offshore-directed current inside the pickup layer. As discussed in detail by van der Zanden et al. (2016), both undertow current and WBL streaming are observed with increasing and decreasing magnitudes, respectively, between 51 m and 54.5 m. For $x\geq$55 m, no onshore WBL streaming can be observed in the sheet flow layer due to the dominant undertow which reaches values up to −0.5 m/s at 55.5 m.

Figure 14e first reveals the much higher magnitudes of the bedload flux at intrawave scale compared to the flux magnitude reached in the upper suspension layer (>1 order of magnitude). In mean, however, this near-bed representation of the fluxes can be misleading, since as shown by van der Zanden, Hurther, et al. (2017) for $x\geq$ 53 m, the net suspended sand transport rate (i.e., covering the entire water column up to the wave crest) and the net bedload transport rate have the same order of magnitude but have opposite direction. This was also shown by Mieras et al. (2017b) for a wider range of shoaling wave conditions.

Figure 14e also shows the strongly positively skewed intrawave sand flux profiles represented by the higher onshore flux magnitude at the wave crest (around t/T = 0.1) compared to the weaker offshore flux at the wave trough (at t/T = 0.8). The corresponding total (bedload plus suspension) net flux profile in Figure 14f reveals a complex three-layer vertical structure of the net sand flux over the first 10 mm above the bed, as superimposed regions of alternating onshore, offshore, and onshore net fluxes. This aspect and its cross-shore dependence is addressed in the following section.

4.3.1. Intrawave and Net Sheet Flow Flux Dynamics

For comparison with results obtained in oscillatory sheet flow by O'Donoghue and Wright (2004b), the vertical structure of the sheet flow sand flux is first investigated on the basis of the net profiles (Figures 15b, 15d, 15f, 15h, and 15j) calculated as follows:

$$\overline{\Phi}(z) = \int_0^1 \Phi(\delta_e \leq z \leq \delta_u, t/T)\mathrm{d}t/T \tag{5}$$

with $\Phi(\delta_e \leq z \leq \delta_u, t/T) = \langle cu \rangle$ as the total intrawave sediment flux restricted to the sheet flow layer (with the $\langle \ldots \rangle$ representing the phase average, used explicitly here; see section 2). The profile obtained at x = 51 m (Figure 15b) shows a simple vertical structure composed of a single onshore-oriented layer extending over the entire sheet flow layer. This type of profile corresponds to the one observed for coarse sand under velocity-skewed oscillatory flows, named type 3 in O'Donoghue and Wright (2004b). In terms of hydrodynamic conditions, this cross-shore position (x = 51 m) in the shoaling region is the closest to oscillatory flow tunnel conditions since wave-breaking effects and undertow currents are weak and the velocity asymmetry transforms into a mainly velocity-skewed flow inside the pickup layer (shown in section 3.4, Figure 3 at x= 51 m). Moreover, if velocity asymmetry is not completely reduced to zero at the bed location, this contributes to an increase in the phase lead of maximum bed shear stress in the crest half cycle, as previously shown by Nielsen (2006) and Ruessink et al. (2011) for skewed asymmetric oscillatory flows. To

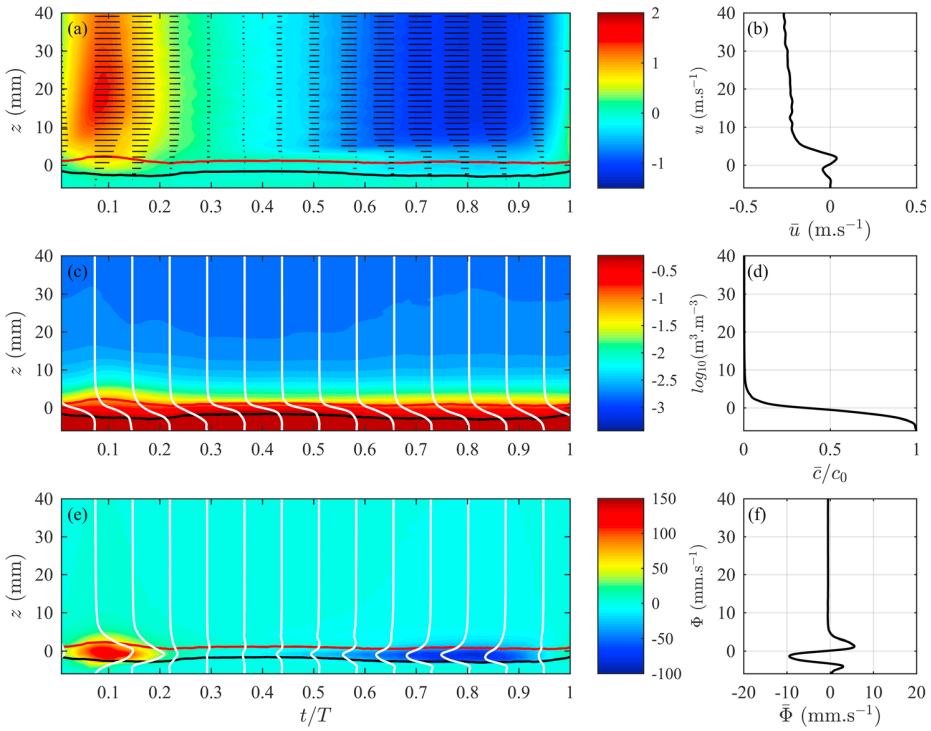

Figure 14. Acoustic Concentration and Velocity Profiler measurements at x = 54.5 m of (a) phase-averaged horizontal velocity field (wave plus current) and velocity vector magnitudes at fixed relative times; (b) time-averaged vertical profiles of horizontal velocity; (c) phase-averaged volumetric concentration field (color bar in log scale) and vertical concentration profiles at fixed relative times (white lines, in linear scale); (d) time-averaged concentration profile; (e) phase-averaged (total) horizontal sediment flux field (color contour) and vertical profiles of horizontal sediment flux at fixed relative times (white lines); (f) vertical profile of time-averaged total sediment flux. All color plots include the averaged undisturbed bed level (black line) and suspension interface (red line).

conclude on the hydrodynamic difference with oscillatory flow, in the absence of phase lag effects, onshore-directed WBL streaming under progressive waves contributes to onshore sand transport, as supported by the profile shape in Figure 15b.

The absence of phase lag effects suggested by the profile shape at x = 51 m differs from the observations made by O'Donoghue and Wright (2004b) for well-sorted medium-sized sand. In order to verify this aspect, Figures 15b, 15d, 15f, 15h, and 15j show the profiles of net sheet flow sand flux decomposed by

$$\overline{uc} = \overline{u}\,\overline{c} + \overline{\tilde{u}\tilde{c}} + \overline{u'c'} \tag{6}$$

where the three terms on the right-hand side of equation (6) correspond to the current, wave, and turbulence contributions to the flux. First, it can be seen that at x = 51 m, the current and turbulent sand fluxes are weaker than the wave-driven flux, except in the pickup layer where the onshore-directed current dominates. Second, the wave-driven flux is fully onshore-directed, which is expected for skewed waves in the absence of concentration phase lag effects. This specific point can be analyzed by the representation in Figures 15a, 15c, 15e, 15g, and 15i of the depth-integrated intrawave sheet flow flux, calculated as

$$\widehat{\Phi}(t/T) = \int_{\delta_e(t/T)}^{\delta_u(t/T)} \Phi(z, t/T)\mathrm{d}z \tag{7}$$

O'Donoghue and Wright (2004b) demonstrated that despite strongly velocity-skewed oscillatory flows, phase lag effects reduce the sand flux asymmetry between the positive and negative flow half cycles because of the transport in the offshore direction of (fine) sand picked up during the more dynamic positive flow half cycle. It can be seen in Figures 15a, 15c, 15e, 15g, and 15i that the strong asymmetry between the crest and trough

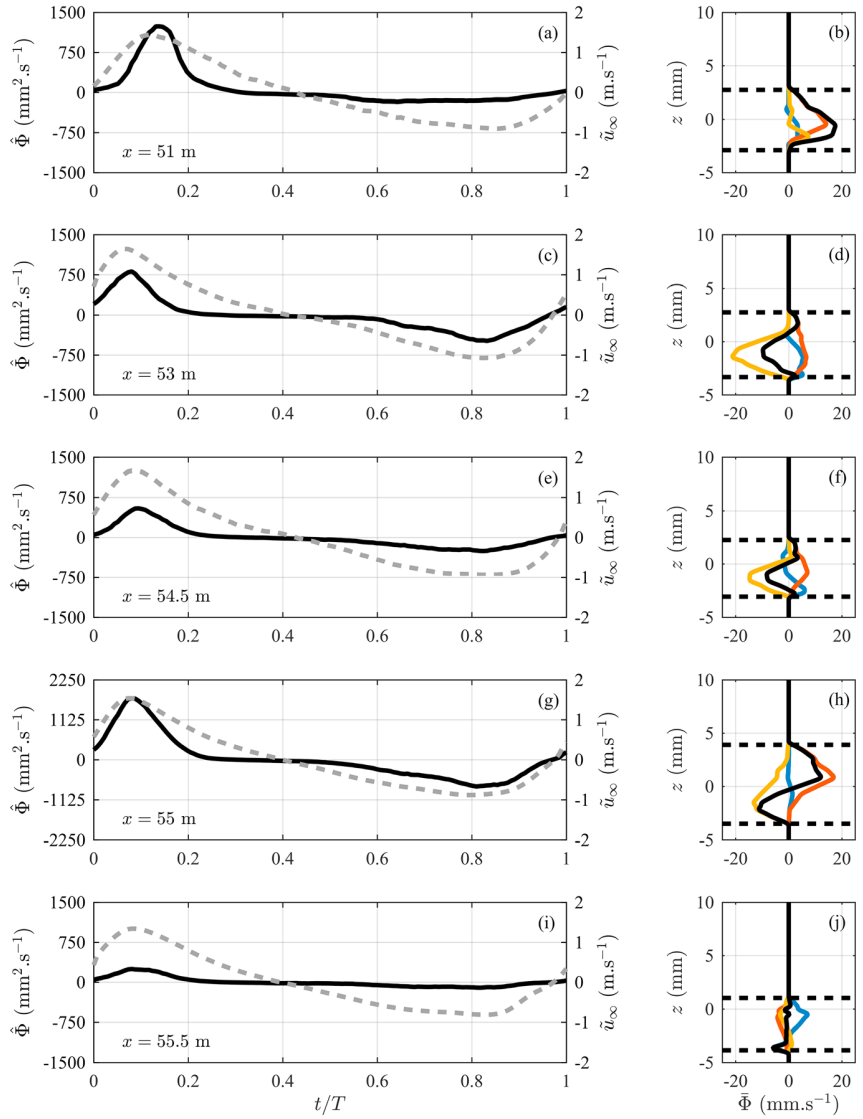

Figure 15. (a, c, e, g) Intrawave fluxes in the sheet flow layer (i.e., vertically integrated) at each cross-shore position between $x = 51$ m and $x = 55.5$ m (solid black lines) and corresponding free-stream orbital velocity (dashed gray lines); (b, d, f, h) time-averaged sediment flux profiles (black solid line) limited to the sheet flow layer, and its decomposition into orbital (orange solid line), current (yellow solid line), and turbulent (blue solid line) components. Note the different vertical scale for panel (g).

flux suggest an absence of strong phase lag effects for the present experiment. Additionally, no peak in concentration was measured around the flow reversal, as identified in (for example) Foster et al. (1994) as a possible consequence of shear instability effects in oscillatory sheet flows before flow reversal.

The profiles of total flux observed at $x = 53$ m to $x = 55$ m (solid black lines in Figures 15d, 15f, and 15h) exhibit similarly shaped profiles of more complex vertical structure, consisting of three distinct layers: (i) an onshore-directed lowest layer, which varies in thickness depending on the cross-shore position (maximum at $x = 54.5$ m where it covers the entire pickup layer) followed by (ii) an offshore-directed layer (maximum at $x = 55$ m where it covers the upper part of the pickup layer and a fraction of the upper sheet flow layer), and (iii) an onshore-directed layer at the transition between the sheet flow and suspension layers. At $x = 55$ m, the near-bed turbulence-driven component is weaker close to the bed, which results in a negligible net onshore flux, giving the appearance of a two-layer structure with the thickness of the lowest layer nearly

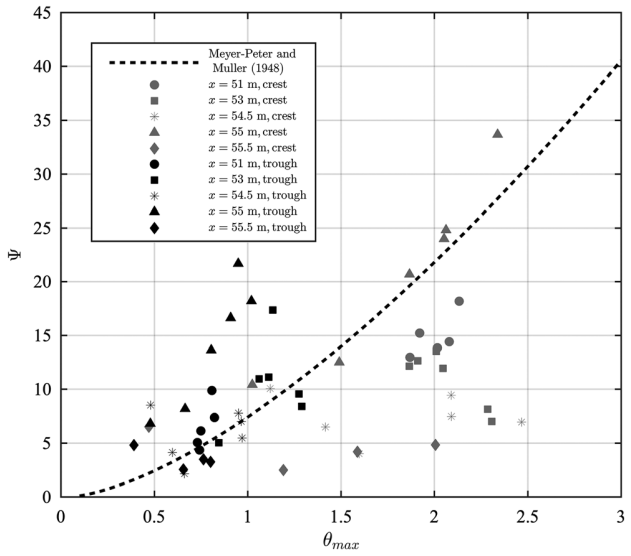

Figure 16. Calculated onshore- (black symbols) and offshore-averaged (gray symbols) dimensionless net flux versus the effective onshore and offshore Shields numbers at each cross-shore position. Meyer-Peter and Müller (1948) formulation is included in the plot (equation (11), black dashed line).

zero. Following the profile classification proposed in O'Donoghue and Wright (2004b), this shape is identical to their type 2 for sheet flows of medium-sized sands. Whether the layer of offshore-directed net flux is here induced by phase lag effects is explored from the decomposed net fluxes presented in Figures 15b, 15d, 15f, 15h, and 15j. It can be seen that the change in vertical structure at x = 53 to 55 m, relative to x = 51 m, results from the higher offshore-directed undertow current at these locations. All wave-driven and turbulent fluxes remain onshore-directed over the entire sheet flow layer. In the upper sheet flow and lower pickup layers, the wave plus turbulence induced flux dominates the total flux, while the current-driven flux is stronger in between. The result is a complex three-layer structure of the net total flux with altering directions. The intrawave sheet flow fluxes at x = 53 m to x = 55 m show a reduced asymmetry between crest and trough levels compared to x = 51 m, despite the strong velocity skewness. This possibly relates to the offshore-directed undertow, which leads to an increase in bed shear stress during the offshore half cycle and a reduction in bed shear stress during the onshore half cycle.

At x = 55.5 m, the intrawave flux and the vertical profile of time-averaged flux (Figures 15i and 15j) differ greatly in shape and magnitude compared to the corresponding results for the other locations. The intrawave flux in Figure 15i reveals strongly reduced wave-driven flux at intrawave scale compared to the other locations, due to a reduced orbital amplitude as a result of breaking-induced wave energy dissipation. The net total flux is close to zero as a consequence of high onshore-directed turbulent sand flux, compensating the sum of the offshore-directed wave- and undertow-driven flux. The turbulent sand flux may be linked to the wave plunger impact, but locally bed-friction-generated turbulence may be equally important since the net turbulent flux magnitudes at x = 55.5 m are similar to those observed at the other cross-shore locations.

4.3.2. Net Bedload Transport Rates

In order to test if wave breaking affects predictions of net bedload transport rate, the half-wave-averaged sediment transport rates Q_c (crest) and Q_t (trough) inside the sheet flow layer are calculated as

$$Q_c = \frac{1}{T_c}\int_0^{T_c}\int_{\delta_e(t)}^{\delta_u(t)} \Phi(z,t)\mathrm{d}z\mathrm{d}t \tag{8}$$

$$Q_t = \frac{1}{T_t}\int_{T_c}^{T}\int_{\delta_e(t)}^{\delta_u(t)} \Phi(z,t)\mathrm{d}z\mathrm{d}t \tag{9}$$

where the spatial integral corresponds to the intrawave net sheet flow flux represented in Figure 15. From these quantities, the corresponding normalized half-wave-averaged transport rates are estimated as

$$\Psi_{c/t} = \frac{|\,Q_{c/t}\,|}{\sqrt{(s-1)gd_{50}^3}} \tag{10}$$

with g = 9.81 m/s^2 the acceleration due to gravity and s the ratio of sediment to water density. This methodology of net (half-wave cycle) transport rate calculation has recently been applied by Cheng et al. (2017) to explore the impact of momentary bed failure effects in oscillatory sheet flows. The values obtained here for all runs and cross-shore positions are compared in Figure 16 to the well-known Meyer-Peter and Müller (1948) formulation (MPM) for bedload transport, given by

$$\Psi = M_0(\theta_{\max} - \theta_c)^{N_0} \tag{11}$$

This model is considered to be accurate when bed friction drives bedload transport and in the absence of bed forms (as in the conditions studied herein). In equation (11), θ_c = 0.05 represents the critical Shields number value for the medium-sized sand used here. Values of M_0 = 8 and N_0 = 1.5, as originally proposed by

Meyer-Peter and Müller (1948), are used because more recently proposed values (e.g., Ribberink, 1998) do not give an overall better agreement. The Shields number used in equation (11) for the model-predicted half-cycle sediment fluxes is calculated as in section 4.1.

Rather than assessing the predictive power of MPM predictor, the present comparison between measured (equation (10)) and predicted (equation (11)) sand transport rates aims to qualify whether (or not) bed friction drives bedload transport, thus suggesting weak (potential) impact from the wave breaking on the bedload transport. First, it can be seen in Figure 16 that the measured transport rates at $x = 51$ m and $x = 53$ m give the best agreement with the MPM predictor, for both crest and trough flux, in spite of the relative scatter of the data. This is likely due to the bedload transport being locally controlled by bed friction processes, with negligible effect from the wave breaking. At $x = 54.5$ m, the trough-averaged flux is still in reasonable agreement with MPM but the crest values become systematically lower than the MPM predictions by more than a factor of 2. The crest value discrepancy becomes maximum at $x = 55.5$ m under the impact of the plunger except at $x = 55$ m, where large discrepancies affect the trough-averaged fluxes that are larger than the model results, rather than crest associated values. It can be deduced from Figure 16 that for $x \geq 54.5$ m, wave breaking is suspected to have substantial effects on bedload transport (van der Zanden et al., 2016, 2018), hence the poor agreement of the MPM predictor at these cross-shore locations; an improved predictor would require velocity asymmetry and breaking-induced effects to be included in a parametrized way.

5. Conclusions

WBL hydrodynamics and sheet flow properties have been investigated under regular, large-scale, plunging-type breaking waves using acoustic high-resolution profile measurements of velocities and sand concentrations provided by the ACVP technology. Because acoustic measurements are usually limited to suspension layer profiling, a validation of the acoustic sheet flow measurements was first carried out using CCM+ data as reference measurements, collected at a fixed position in the outer surf zone. The acoustic measurement of intrawave and maximum erosion depth, as well as the sheet flow layer thickness, were found to be in good quantitative agreement with the CCM+ measurements. The intrawave concentration fields depict similar internal sheet flow dynamics as the CCM+, showing antiphase and in-phase behaviors in the pickup and upper sheet flow layers, respectively. The direct acoustic estimation of the net sheet flow transport rate was within 25% of that estimated using the CCM+. Considering the much lower spatial resolution of the acoustic technology (1.5 mm) and the very different sampling and averaging methodologies applied in the two measurement systems, this level of agreement is considered to validate the acoustic sheet flow measurements. The ACVP was subsequently used to measure WBL hydrodynamics and sheet flow processes at five cross-shore locations across the outer wave-breaking region over a medium-sand breaker bar. The following are the main results for the hydrodynamics:

1. The free-stream intrawave velocity measurements reveal the presence of strongly skewed asymmetric waves across the wave-breaking region. The maximum intrawave WBL thickness is found to be slightly lower during the short-duration wave crest half cycles than during the longer-duration trough half cycles as expected in the presence of skewed asymmetrical waves.
2. For all cross-shore positions, the measured first harmonic velocity phase lead φ lies in the range of 10–20°. When presented as a function of local dimensionless semiexcursion a/k_s in comparison to existing full-scale oscillatory sheet flow data found in the literature, the measured φ values lie in the region of the logarithmic decay as seen in Figure 5 (van der A et al., 2011). This confirms a fully turbulent flow regime across the wave-breaking region.
3. The wave nonlinearity transformation inside the WBL is tested quantitatively by the application of the model proposed by Henderson et al. (2004). The model-predicted ratio of near-bed to free-stream velocity skewness was found to follow the measured value with a mean overestimation of 18% for all positions across the studied wave-breaking region. This level of agreement is attributed to the fully established turbulent flow regime at all cross-shore positions. This flow regime is representative for breaking waves in the natural environment.

   The following are the main results for the sheet flow sediment dynamics:
4. Erosion depth and sheet flow layer thickness exhibit similar intrawave dynamics as previously observed in flow tunnel experiments with skewed oscillatory sheet flows. The internal sheet flow layer structure

reveals the existence of a lower pickup layer and an upper sheet flow layer. The top of the pickup layer corresponds to the height of minimal intrawave concentration variability, which corresponds to the location of a pivotal point in the intrawave concentration profiles.

5. Pivot point elevation and time-averaged concentration at the pivot point are in good agreement with the corresponding values reported by O'Donoghue and Wright (2004b) for skewed oscillatory flow sheet flows. However, at the plunge point, the pivot elevation is higher and the time-averaged concentration is lower compared to the measurements at the other cross-shore locations. At this plunge point, van der Zanden et al. (2018) recently showed that the plunging breaker-induced turbulent kinetic energy is affecting the entire water column down into the bottom WBL (see their Figures 5i and 5j) confirming locally increased turbulent mixing affecting the sheet flow layer. Making use of the full measurement performance of the ACVP technology, the total sheet flow sand transport rate was decomposed into current-, wave- and turbulence-driven components, with the following main results:
6. In the shoaling zone, the time-averaged sediment flux profile exhibits a single layer vertical structure of purely onshore-directed transport over the entire sheet flow layer. This total transport is shown to be dominated by the wave-driven component, with negligible current and turbulence-driven contributions. Furthermore, the onshore-directed wave-driven transport and the positively skewed intrawave bedload transport rate strongly suggest the absence of phase lag effects in these experiments.
7. In the outer surf zone, except at the location of the plunge point, the net flux profile in the sheet flow layer is composed of a three-layer vertical structure with alternating onshore-, offshore- and onshore-directed layers. The offshore-directed flux layer is driven by the undertow, not by phase lag effects.
8. At the plunge point, the turbulence-driven onshore component balances the combined contributions of the offshore-directed wave- and undertow-driven components, resulting in a negligibly low net bedload sand transport rate. Compared to the other positions, this is attributed mainly to the strong reduction of the wave-driven sand flux as a possible consequence of breaking-induced wave energy dissipation via turbulent cascading processes (see Figure 11a in van der Zanden et al., 2018).
9. Applying the same methodology as Cheng et al. (2017), the half-cycle net bedload transport rate was compared to predicted net transport using the Meyer-Peter and Müller (1948) formula. For the farthest offshore positions (x = 51 m and x = 53 m), the crest- and trough- transport rates are in relative good agreement with the empirical model predictions. Elsewhere, the agreement is less good, indicating that a solely bed friction-based bedload model is inadequate for the present study conditions, where additional factors such as wave breaking may influence bedload transport.

The detailed hydrodynamic WBL and sheet flow measurements reported here under large-scale breaking waves constitute a useful high-resolution data set for the improvement and validation of fine-scale numerical simulations of cross-shore sand transport in an energetic wave-breaking region.

Acknowledgments
The authors wish to thank the staff of CIEMLAB, in particular, Joaquim Sospedra, Oscar Galego, and Ricardo Torres, for their hospitality and hard work during the experimental campaign. This research was funded by the European Community's Horizon 2020 Programme through the Integrated Infrastructure Initiative HYDRALAB+ COMPLEX (654110), the French DGA-funded ANR Astrid Maturation project MESURE (ANR-16-ASMA-0005-01), the SINBAD project funded by STW (12058) in the Netherlands, and by EPSRC (EP/J00507X/1, EPJ005541/1) in the UK. Data of this study are available at U. Twente repository doi: (http://dx.doi.org/10.4121/uuid:7882a515-2097-4639-a756-d2961d3dd593). Comments and remarks raised by the two anonymous reviewers helped to improve the quality of the paper.

References

Amoudry, L., Hsu, T.-J., & Liu, P. L.-F. (2008). Two-phase model for sand transport in sheet flow regime. *Journal of Geophysical Research*, *113*, C03011. https://doi.org/10.1029/2007JC004179

Anderson, D., Cox, D., Mieras, R., Puleo, J. A., & Hsu, T.-J. (2017). Observations of wave-induced pore pressure gradients and bed level response on a surf zone sandbar. *Journal of Geophysical Research: Oceans*, *122*, 5169–5193. https://doi.org/10.1002/2016JC012557

Bailard, J. A. (1981). An energetics total load sediment transport model for a plane sloping beach. *Journal of Geophysical Research*, *86*(C11), 10,938–10,954. https://doi.org/10.1029/JC086iC11p10938

Battjes, J. A. (1975). Surf similarity. In Coastal Engineering 1974 (pp. 466–480).

Berni, C., Barthélemy, E., & Michallet, H. (2013). Surf zone cross-shore boundary layer velocity asymmetry and skewness: An experimental study on a mobile bed. *Journal of Geophysical Research: Oceans*, *118*, 2188–2200. https://doi.org/10.1002/jgrc.20125

Caliskan, U., & Fuhrman, D. R. (2017). RANS-based simulation of wave-induced sheet-flow transport of graded sediments. *Coastal Engineering*, *121*, 90–102. https://doi.org/10.1016/j.coastaleng.2016.11.007

Chassagneux, F. X., & Hurther, D. (2014). Wave bottom boundary layer processes below irregular surfzone breaking waves with light-weight sheet flow particle transport. *Journal of Geophysical Research: Oceans*, *119*, 1668–1690. https://doi.org/10.1002/2013JC009338

Cheng, Z., Hsu, T.-J., & Calantoni, J. (2017). SedFoam: A multi-dimensional Eulerian two-phase model for sediment transport and its application to momentary bed failure. *Coastal Engineering*, *119*, 32–50. https://doi.org/10.1016/j.coastaleng.2016.08.007

Dibajnia, M., & Watanabe, A. (1998). Transport rate under irregular sheet flow conditions. *Coastal Engineering*, *35*(3), 167–183. https://doi.org/10.1016/S0378-3839(98)00034-9

Dick, J. E., & Sleath, J. F. A. (1992). Sediment transport in oscillatory sheet flow. *Journal of Geophysical Research*, *97*(C4), 5745–5758. https://doi.org/10.1029/92JC00054

Dixen, M., Hatipoglu, F., Sumer, B. M., & Fredsøe, J. (2008). Wave boundary layer over a stone-covered bed. *Coastal Engineering*, *55*(1), 1–20. https://doi.org/10.1016/j.coastaleng.2007.06.005

Doering, J. C., & Bowen, A. J. (1995). Parametrization of orbital velocity asymmetries of shoaling and breaking waves using bispectral analysis. *Coastal Engineering*, *26*(1–2), 15–33. https://doi.org/10.1016/0378-3839(95)00007-X

Dohmen-Janssen, C. M., & Hanes, D. M. (2002). Sheet flow dynamics under monochromatic nonbreaking waves. *Journal of Geophysical Research*, *107*(C10), 3149. https://doi.org/10.1029/2001JC001045

Dohmen-Janssen, C. M., & Hanes, D. M. (2005). Sheet flow and suspended sediment due to wave groups in a large wave flume. *Continental Shelf Research*, *25*(3), 333–347. https://doi.org/10.1016/j.csr.2004.10.009

Dohmen-Janssen, C. M., Hassan, W. N., & Ribberink, J. S. (2001). Mobile-bed effects in oscillatory sheet flow. *Journal of Geophysical Research*, *106*(C11), 27–103.

Drake, T. G., & Calantoni, J. (2001). Discrete particle model for sheet flow sediment transport in the nearshore. *Journal of Geophysical Research*, *106*(C9), 19,859–19,868. https://doi.org/10.1029/2000JC000611

Elgar, S. (1987). Relationships involving third moments and bispectra of a harmonic process. *IEEE Transactions on Acoustics, Speech, and Signal Processing*, *35*(12), 1725–1726. https://doi.org/10.1109/TASSP.1987.1165090

Fernández-Mora, A., Calvete, D., Falqués, A., & Swart, H. E. (2015). Onshore sandbar migration in the surf zone: New insights into the wave-induced sediment transport mechanisms. *Geophysical Research Letters*, *42*, 2869–2877. https://doi.org/10.1002/2014GL063004

Finn, J. R., Li, M., & Apte, S. V. (2016). Particle based modelling and simulation of natural sand dynamics in the wave bottom boundary layer. *Journal of Fluid Mechanics*, *796*, 340–385.

Foster, D. L., Holman, R. A., & Beach, R. A. (1994). Sediment suspension events and shear instabilities in the bottom boundary layer. In *Proc. Coastal Dynamics '94*, (pp. 712–726). Barcelona, Spain: ASCE.

Fromant, G., Mieras, R., Revil-Baudard, T., Puleo, J., Hurther, D., & Chauchat, J. (2018). On bedload and suspended load measurement performances in sheet flows using acoustic and conductivity profilers. *Journal of Geophysical Research: Earth Surface*, *123*, 2546–2562. https://doi.org/10.1029/2017JF004560

Fuhrman, D. R., Fredsøe, J., & Sumer, B. M. (2009). Bed slope effects on turbulent wave boundary layers: 2. Comparison with skewness, asymmetry, and other effects. *Journal of Geophysical Research*, *114*, C03025. https://doi.org/10.1029/2008JC005045

Fuhrman, D. R., Schløer, S., & Sterner, J. (2013). RANS-based simulation of turbulent wave boundary layer and sheet-flow sediment transport processes. *Coastal Engineering*, *73*, 151–166. https://doi.org/10.1016/j.coastaleng.2012.11.001

Hassan, W. N., & Ribberink, J. S. (2005). Transport processes of uniform and mixed sands in oscillatory sheet flow. *Coastal Engineering*, *52*(9), 745–770. https://doi.org/10.1016/j.coastaleng.2005.06.002

Henderson, S. M., Allen, J. S., & Newberger, P. A. (2004). Nearshore sandbar migration predicted by an eddy-diffusive boundary layer model. *Journal of Geophysical Research*, *109*, C06024. https://doi.org/10.1029/2003JC002137

Henriquez, M., Reniers, A., Ruessink, B. G., & Stive, M. J. F. (2014). PIV measurements of the bottom boundary layer under nonlinear surface waves. *Coastal Engineering*, *94*, 33–46. https://doi.org/10.1016/j.coastaleng.2014.08.004

Hoefel, F., & Elgar, S. (2003). Wave-induced sediment transport and sandbar migration. *Science*, *299*(5614), 1885–1887. https://doi.org/10.1126/science.1081448

Horikawa, K., Watanabe, A., & Katori, S. (1982). Sediment transport under sheet flow condition. *Coastal Engineering Proceedings*, *1*(18), 1335–1352.

Hsu, T.-J., & Liu, P. L.-F. (2004). Toward modeling turbulent suspension of sand in the nearshore. *Journal of Geophysical Research*, *109*, C06018. https://doi.org/10.1029/2003JC002240

Hurther, D., & Thorne, P. D. (2011). Suspension and near-bed load sediment transport processes above a migrating, sand-rippled bed under shoaling waves. *Journal of Geophysical Research*, *116*, C07001. https://doi.org/10.1029/2010JC006774

Hurther, D., Thorne, P. D., Bricault, M., Lemmin, U., & Barnoud, J.-M. (2011). A multi-frequency acoustic concentration and velocity profiler (ACVP) for boundary layer measurements of fine-scale flow and sediment transport processes. *Coastal Engineering*, *58*(7), 594–605. https://doi.org/10.1016/j.coastaleng.2011.01.006

Jonsson, I. G. (1980). A new approach to oscillatory rough turbulent boundary layers. *Ocean Engineering*, *7*(1), 109–152. https://doi.org/10.1016/0029-8018(80)90034-7

King Jr, D. B. (1991). Studies in oscillatory flow bedload sediment transport, (PhD thesis). University of California, San Diego, 184pp.

Kranenburg, W. M., Hsu, T.-J., & Ribberink, J. S. (2014). Two-phase modeling of sheet-flow beneath waves and its dependence on grain size and streaming. *Advances in Water Resources*, *72*, 57–70. https://doi.org/10.1016/j.advwatres.2014.05.008

Kranenburg, W. M., Ribberink, J. S., Schretlen, J. J. L. M., & Uittenbogaard, R. E. (2013). Sand transport beneath waves: The role of progressive wave streaming and other free surface effects. *Journal of Geophysical Research: Earth Surface*, *118*, 122–139. https://doi.org/10.1029/2012JF002427

Lanckriet, T., Puleo, J., Masselink, G., Turner, I., Conley, D., Blenkinsopp, C., & Russell, P. (2014). Comprehensive field study of swash-zone processes. II: Sheet flow sediment concentrations during quasi-steady-backwash. *Journal of Waterway, Port, Coastal, and Ocean Engineering*, *140*(1), 29–42. https://doi.org/10.1061/(ASCE)WW.1943-5460.0000209

McLean, S. R., Ribberink, J. S., Dohmen-Janssen, C. M., & Hassan, W. N. (2001). Sand transport in oscillatory sheet flow with mean current. *Journal of Waterway, Port, Coastal, and Ocean Engineering*, *127*(3), 141–151. https://doi.org/10.1061/(ASCE)0733-950X(2001)127:3(141)

Meyer-Peter, E., & Müller, R. (1948). Formulas for bed-load transport. Proceedings of the 2nd Meeting of the International Association of Hydraulic Research, 39–64. https://doi.org/1948-06-07

Mieras, R., Puleo, J. A., Anderson, D., Cox, D. T., & Hsu, T.-J. (2017b). Large-scale experimental observations of wave-induced sediment transport over a surf zone sandbar. In Proceeding of 18th International Conference of Coastal Dynamics, Helsingør, Denmark (pp. 618–629).

Mieras, R. S., Puleo, J. A., Anderson, D., Cox, D. T., & Hsu, T.-J. (2017a). Large-scale experimental observations of sheet flow on a sandbar under skewed-asymmetric waves. *Journal of Geophysical Research: Oceans*, *122*, 5022–5045. https://doi.org/10.1002/2016JC012438

Naqshband, S., Ribberink, J. S., Hurther, D., Barraud, P.-A., & Hulscher, S. (2014). Experimental evidence for turbulent sediment flux constituting a large portion of the total sediment flux along migrating sand dunes. *Geophysical Research Letters*, *41*, 8870–8878. https://doi.org/10.1002/2014GL062322

Naqshband, S., Ribberink, J. S., Hurther, D., & Hulscher, S. (2014). Bed load and suspended load contributions to migrating sand dunes in equilibrium. *Journal of Geophysical Research: Earth Surface*, *119*, 1043–1063. https://doi.org/10.1002/2013JF003043

Nielsen, P. (1992). *Coastal bottom boundary layers and sediment transport* (Vol. 4). Singapore: World Scientific Publishing Co Inc.

Nielsen, P. (2006). Sheet flow sediment transport under waves with acceleration skewness and boundary layer streaming. *Coastal Engineering*, *53*(9), 749–758. https://doi.org/10.1016/j.coastaleng.2006.03.006

Nielsen, P. (2016). 1DV structure of turbulent wave boundary layers. *Coastal Engineering*, *112*(1–8), 1–8. https://doi.org/10.1016/j.coastaleng.2016.02.001

Nielsen, P., & Callaghan, D. (2003). Shear stress and sediment transport calculations for sheet flow under waves. *Coastal Engineering*, *47*(3), 347–354. https://doi.org/10.1016/S0378-3839(02)00141-2

Nielsen, P., van der Wal, K., & Gillan, L. (2002). Vertical fluxes of sediment in oscillatory sheet flow. *Coastal Engineering*, *45*(1), 61–68. https://doi.org/10.1016/S0378-3839(01)00043-6

O'Donoghue, T., & Wright, S. (2004a). Concentrations in oscillatory sheet flow for well sorted and graded sands. *Coastal Engineering*, *50*(3), 117–138. https://doi.org/10.1016/j.coastaleng.2003.09.004

O'Donoghue, T., & Wright, S. (2004b). Flow tunnel measurements of velocities and sand flux in oscillatory sheet flow for well-sorted and graded sands. *Coastal Engineering*, *51*(11-12), 1163–1184. https://doi.org/10.1016/j.coastaleng.2004.08.001

Revil-Baudard, T., Chauchat, J., Hurther, D., & Barraud, P.-A. (2015). Investigation of sheet-flow processes based on novel acoustic high-resolution velocity and concentration measurements. *Journal of Fluid Mechanics*, *767*, 1–30. https://doi.org/10.1017/jfm.2015.23

Revil-Baudard, T., Chauchat, J., Hurther, D., & Eiff, O. (2016). Turbulence modifications induced by the bed mobility in intense sediment-laden flows. *Journal of Fluid Mechanics*, *808*, 469–484. https://doi.org/10.1017/jfm.2016.671

Ribberink, J. S. (1998). Bed-load transport for steady flows and unsteady oscillatory flows. *Coastal Engineering*, *34*(1-2), 59–82. https://doi.org/10.1016/S0378-3839(98)00013-1

Ribberink, J. S., & Al-Salem, A. A. (1994). Sediment transport in oscillatory boundary layers in cases of rippled beds and sheet flow. *Journal of Geophysical Research*, *99*(C6), 12,707–12,727. https://doi.org/10.1029/94JC00380

Ribberink, J. S., der Werf, J. J., O'Donoghue, T., & Hassan, W. N. M. (2008). Sand motion induced by oscillatory flows: Sheet flow and vortex ripples. *Journal of Turbulence*, *9*(20), 1–32. https://doi.org/10.1080/14685240802220009

Ribberink, J. S., Dohmen-Janssen, C. M., Hanes, D. M., McLean, S. R., & Vincent, C. (2001). Near-bed sand transport mechanisms under waves—A large-scale flume experiment (Sistex99). In Coastal Engineering 2000 (pp. 3263–3276).

Ruessink, B. G., Michallet, H., Abreu, T., Sancho, F., van der A, D. A., van der Werf, J. J., & Silva, P. A. (2011). Observations of velocities, sand concentrations, and fluxes under velocity-asymmetric oscillatory flows. *Journal of Geophysical Research*, *116*, C03004. https://doi.org/10.1029/2010JC006443

Schretlen, J. J. L. M., Ribberink, J. S., & O'Donoghue, T. (2009). Sand transport under full-scale surface waves. In Proceedings of Coastal Dynamics 2009: Impacts of Human Activities on Dynamic Coastal Processes (With CD-ROM) (pp. 1–13). World Scientific.

Schretlen, J. L. M. (2012). *Sand transport under full-scale progressive surface waves* (PhD thesis). Netherlands: Universiteit Twente.

Sumer, B. M., Kozakiewicz, A., Fredsøe, J., & Deigaard, R. (1996). Velocity and concentration profiles in sheet-flow layer of movable bed. *Journal of Hydraulic Engineering*, *122*(10), 549–558. https://doi.org/10.1061/(ASCE)0733-9429(1996)122:10(549)

Thorne, P. D., & Hanes, D. M. (2002). A review of acoustic measurement of small-scale sediment processes. *Continental Shelf Research*, *22*(4), 603–632. https://doi.org/10.1016/S0278-4343(01)00101-7

Thorne, P. D., & Hurther, D. (2014). An overview on the use of backscattered sound for measuring suspended particle size and concentration profiles in non-cohesive inorganic sediment transport studies. *Continental Shelf Research*, *73*, 97–118. https://doi.org/10.1016/j.csr.2013.10.017

Thorne, P. D., Hurther, D., & Moate, B. D. (2011). Acoustic inversions for measuring boundary layer suspended sediment processes. *The Journal of the Acoustical Society of America*, *130*(3), 1188–1200. https://doi.org/10.1121/1.3618728

van der A, D. A., O'Donoghue, T., Davies, A. G., & Ribberink, J. S. (2011). Experimental study of the turbulent boundary layer in acceleration-skewed oscillatory flow. *Journal of Fluid Mechanics*, *684*, 251–283. https://doi.org/10.1017/jfm.2011.300

van der A, D. A., O'Donoghue, T., & Ribberink, J. S. (2010). Measurements of sheet flow transport in acceleration-skewed oscillatory flow and comparison with practical formulations. *Coastal Engineering*, *57*(3), 331–342. https://doi.org/10.1016/j.coastaleng.2009.11.006

van der A, D. A., Ribberink, J. S., van der Werf, J. J., O'Donoghue, T., Buijsrogge, R. H., & Kranenburg, W. M. (2013). Practical sand transport formula for non-breaking waves and currents. *Coastal Engineering*, *76*, 26–42. https://doi.org/10.1016/j.coastaleng.2013.01.007

van der A, D. A., van der Zanden, J., O'Donoghue, T., Hurther, D., Cáceres, I., McLelland, S. J., & Ribberink, J. S. (2017). Large-scale laboratory study of breaking wave hydrodynamics over a fixed bar. *Journal of Geophysical Research: Oceans*, *122*, 3287–3310. https://doi.org/10.1002/2016JC012072

van der Zanden, J., Alsina, J. M., Cáceres, I., Buijsrogge, R. H., & Ribberink, J. S. (2015). Bed level motions and sheet flow processes in the swash zone: Observations with a new conductivity-based concentration measuring technique (CCM+). *Coastal Engineering*, *105*, 47–65. https://doi.org/10.1016/j.coastaleng.2015.08.009

van der Zanden, J., van der A, D. A., Cáceres, I., Hurther, D., McLelland, S. J., Ribberink, J. S., & O'Donoghue, T. (2018). Near-bed turbulent kinetic energy budget under a large-scale plunging breaking wave over a fixed bar. *Journal of Geophysical Research: Oceans*, *123*, 1–28. https://doi.org/10.1002/2017JC01341

van der Zanden, J., van der A, D. A., Hurther, D., Cáceres, I., O'Donoghue, T., & Ribberink, J. S. (2017). Suspended sediment transport around a large-scale laboratory breaker bar. *Coastal Engineering*, *125*, 51–69. https://doi.org/10.1016/j.coastaleng.2017.03.007

van der Zanden, J., van der A, D. A., Hurther, D., Caceres, I., O'Donoghue, T., Hulsher, S. J. M. H., & Ribberink, J. S. (2017). Bedload and suspended load contributions to breaker bar morphopdynamics. *Coastal Engineering*, *129*, 74–92. https://doi.org/10.1016/j.coastaleng.2017.09.005

van der Zanden, J., van der A, D. A., Hurther, D., Cáceres, I., O'Donoghue, T., & Ribberink, J. S. (2016). Near-bed hydrodynamics and turbulence below a large-scale plunging breaking wave over a mobile barred bed profile. *Journal of Geophysical Research: Oceans*, *121*, 6482–6506. https://doi.org/10.1002/2016JC011909

Watanabe, A., & Sato, S. (2004). A sheet-flow transport rate formula for asymmetric, forward-leaning waves and currents. In Coastal Engineering Conference (Vol. 29, p. 1703). https://doi.org/10.1142/9789812701916_0136